A Study of the Detection of Long-Lived Charged Particles With an Auxiliary Detector Above the ATLAS Muon Spectrometer (ADAM)

by

Joseph Mitchell Kelly

A thesis submitted in partial fulfillment of the requirements for the degree of

Master of Science

Department of Physics
University of Alberta

Abstract

The Auxiliary Detector above the ATLAS Muon spectrometer (ADAM) is a proposed particle detector. Its function is to detect the decay products of beyond the standard model (BSM) particles produced in the 14 TeV proton-proton collisions at the Large Hadron Collider (LHC) which evade detection by the ATLAS (A Toroidal LHC ApparatuS) experiment.

Long-lived particles (LLPs) are a feature of many BSM theories. One such model is supersymmetry (SUSY), a theoretical framework that predicts for each boson and fermion in the Standard Model (SM), there may exist a "superpartner" fermion or boson, respectively. In particular, when this model is extended to also include the theoretical graviton particle, which defines "minimal supergravity" (mSUGRA), there is the possibility of a supersymmetric tau lepton, or "stau" with lifetimes of up to a year.

ADAM is a low-cost addition to the existing ATLAS detector to extend its physics reach. This thesis provides a comprehensive simulation of the production, transport and detection of exceptionally long-lived stau particles, that come to rest in the ATLAS detector before decaying, the subsequent decays of these particles can be monitored in a background-free way during planned and unplanned Technical Stops. The ADAM detector is deployed above the ATLAS detector, effectively turning the upper region of the cavern into a 13,000 m^3 fiducial volume for detecting the decays of LLPs. While a particular model and parameter set is used in this work, the resultant heavy charged particle featured in the model is not unique amongst BSM theories, therefore the results may extrapolate to other models. Under the specific scenario

of mSUGRA physics at the LHC during run 4, and based on the cross-section of the $pp \rightarrow \tilde{\tau}\bar{\tilde{\tau}}$ process in the mSUGRA model, the expected integrated luminosity of 715 fb^{-1} over the course of run 4, and the operational schedule of the LHC, our experiment showed up to 132.3 ± 0.9 events recorded by the ADAM detector, and at least three events for stau masses under 148 GeV for all lifetimes, or up to 222 GeV for one year lifetimes.

The only place on earth where immortality is provided is in libraries. This is the collective memory of humanity.

-Temple Grandin

For my parents

Acknowledgements

I would like to acknowledge and thank my advisor Dr. James Pinfold for his guidance in choosing this research topic, the model used, and for sharing his overall knowledge of particle physics with me. I would also like to thank Dr. Jonathan Feng, Dr. Kazuki Sakurai, and Dr. Zach Marshall for their correspondence with me in helping me understand the details of the model used in my research, but also supersymmetry more broadly. I would also like to again thank Dr. Zach Marshall for his help with understanding the software used by the ATLAS project. Many thanks also go to Dr. Marilena Bandieramonte for her email correspondence and replies on the GeoModel github, which enabled me to use FullSimLight and the GeoModel tools, a central part of my thesis. My gratitude also goes to Dr. Axsel Hallin and Dr. Juan Pablo Yanez Garza for agreeing to be on my supervisory committee.

Thank you to Alejandro Salazar Lobos for helping me get adjusted to graduate studies at the University of Alberta, and thank you to Dr. Michael Staelens for help with understanding particle physics monte carlo event generators.

Finally, though I have not spoken to him directly I owe a debt of gratitude to Dr. Mustafa Schmidt for publishing his Geant4 tutorials on YouTube. No singular resource helped me more in completing my Thesis.

Table of Contents

List of Tables

List of Figures

Abbreviations

ADAM Auxiliary Detector above the ATLAS Muon spectrometer.

ALICE A Large Ion Collider Experiment.

ATLAS A Toroidal LHC ApparatuS.

BBN Big Bang Nucleosynthesis.

C2H2F4 tetrafluoroethane.

CAD Computer Aided Design.

CERN European Organization for Nuclear Research.

CF4 Carbon tetraFluoride.

CMB Cosmic Microwave Background.

CMS Compact Muon Solenoid.

CO2 Carbon Dioxide.

CP Charge Parity.

CSC Cathode Strip Chamber.

CTP Central Trigger Processor.

ECAL Electromagnetic Calorimeter.

EM Electromagnetic.

FASER ForwArd Search ExpeRiment.

FSL FullSimLight.

GDML Geometry Description Markup Language.

GEANT4 GEometry ANd Tracking 4.

GeV Giga electron Volt.

HCAL Hadronic Calorimeter.

HL-LHC High Luminosity LHC.

HLT High Level Trigger.

ID Inner Detector.

IP Interaction Point.

kHz kilo Hertz.

kV kilo Volt.

L1 Level 1.

LAr Liquid Argon.

LEP Large Electron-Positron Collider.

LHC Large Hadron Collider.

LHCb LHC beauty.

LHCf LHC forward.

LLP Long-Lived Particle.

LSP Lightest Supersymmetric Particle.

MB Mega Byte.

MDT Monitored Drift Tube.

Mev Mega electron Volt.

MHz Mega Hertz.

MIP Minimum Ionizing Particle.

MoEDAL Monopole and Exotics Detector At the LHC - MoEDAL Apparatus for Penetrating Particles.

MS Muon Spectrometer.

MSSM Minimal Supersymmetric Standard Model.

mSUGRA minimal SUperGRAvity.

n-C5H12 n-pentane.

NbTi Niobium Titanium.

NLSP Next to Lightest Supersymmetric Particle.

ns nano second.

PP Proton-Proton.

PPB Protons-Per Bunch.

PS Proton Synchrotron.

PSB Proton Synchrotron Booster.

QCD Quantum Chromodynamics.

QED Quantum Electrodynamics.

QFT Quantum Field Theory.

RF Radio Frequency.

RGEs Renormalization Group Equations.

RoI Region of Interest.

RPC Resistive Plate Chamber.

SCT Semi-Conductor Tracker.

SD Standard Deviaiton.

SE Standard Error.

SiPM Silicon PhotoMultiplier.

SLHA SUSY Les Houches Accord.

SM Standard Model.

SND Search for Naturalness and Dark matter.

SPS Super Proton Synchrotron.

SQL Structured Query Language.

SU(n) Special Unitary Group - Order n.

SUSY SUperSYmmetry.

TB Tera Byte.

TeV Tera electron Volt.

TGC Thin Gap Chamber.

TOTEM TOTal Elastic and diffractive cross section Measurement.

TRT Transition Radiation Tracker.

U(n) Unitary Group - Order n.

VLLPs Very Long-Lived Particles.

WIMP Weakly Interacting Massive Particle.

Chapter 1

Introduction

The field of particle physics has been significantly advanced by the Large Hadron Collider (LHC), a particle accelerator that has facilitated the exploration of the fundamental constituents of matter. The ATLAS (A Toroidal LHC ApparatuS) experiment [1] at the LHC, together with CMS (Compact Muon Solenoid) [2] discovered the Higgs Boson in 2012 [3][4], the last piece of the Standard Model (SM) puzzle. However, the SM, despite its success in explaining the behaviour and interactions of known elementary particles, does not account for the fundamental parameters of the SM [5], neutrino oscillations [6], the matter-antimatter asymmetry [7] as well as the nature of dark matter and dark energy [8]. Additionally, the SM does not incorporate gravity. These limitations have led to the development of theories Beyond the Standard Model (BSM), one of the most well-studied of which is Supersymmetry (SUSY) [9][10].

SUSY, in its minimal form, proposes a symmetry between fermions and bosons, predicting a supersymmetric partner for each particle in the SM [11]. Among these predicted particles are the staus, the supersymmetric partners of the tau leptons. Certain SUSY models suggest that staus could be very long-lived particles (VLLPs) [12][13][14], with lifetimes on the order of days to years. This characteristic makes them candidates for direct detection in an auxiliary detector in the ATLAS cavern, during operational shutdowns.

This thesis focuses on the simulation of the production of long-lived stau particles at the ATLAS experiment and their subsequent detection in an auxiliary detector named ADAM (Auxiliary Detector above the ATLAS Muon spectrometer), which we are proposing would be positioned above the ATLAS experiment. The simulation is performed using Geant4 [15], a toolkit for the simulation of the passage of particles through matter, and FullSimLight [16], a Geant4 based toolkit used to build and simulate the ATLAS geometry and magnetic field. Geant4 is widely used in high-energy physics for its accurate modelling of particle interactions and detector response.

The primary objective of this work is to evaluate the potential of the ADAM detector to identify and measure the decay products of long-lived stau particles.

The thesis is structured as follows: Chapter 2 provides a theoretical background on the SM and SUSY, with a discussion on the model parameters that could lead to the production of long-lived stau particles. Chapter 3 describes the LHC and the AT-LAS experiment. Chapter 4 introduces the ADAM detector and its design, presents the Geant4 and FullSimLight toolkits and the specific methods used to simulate the production and detection of stau particles. Chapter 5 discusses the results of the simulation and their implications for detecting long-lived particles at the LHC. Finally, Chapter 6 provides a summary of the work and suggestions for future research.

Chapter 2

Theory

2.1 The Standard Model

2.1.1 Overview

The Standard Model (SM) of particle physics presents a comprehensive mathematical framework that describes the fundamental particles and their interactions. The description of the SM that follows is a synthesis of the work in [17][18][5][19]. The SM describes the matter of the universe as fermions, characterized by their distinct spin quantum number of 1/2. Fermions then fall into two further classes: leptons and quarks. Each of these classes consists of three generations, ordered by increasing mass. The lepton generations encompass the electron, the muon, and the tau lepton, each accompanied by a corresponding neutrino. The quark generations include the down and up quarks, the strange and charm quarks, and finally, the bottom and top quarks.

Fermions experience interactions with themselves and other particles through interactions we refer to as forces. The SM describes three fundamental forces: electromagnetism which we experience as the force that binds together atoms into the macroscopic objects we interact with on a daily basis, the strong nuclear force, which binds together the nucleus of atoms, and the weak nuclear force, responsible for the radioactive decay of materials. The remaining force, gravity, is not described by the SM.
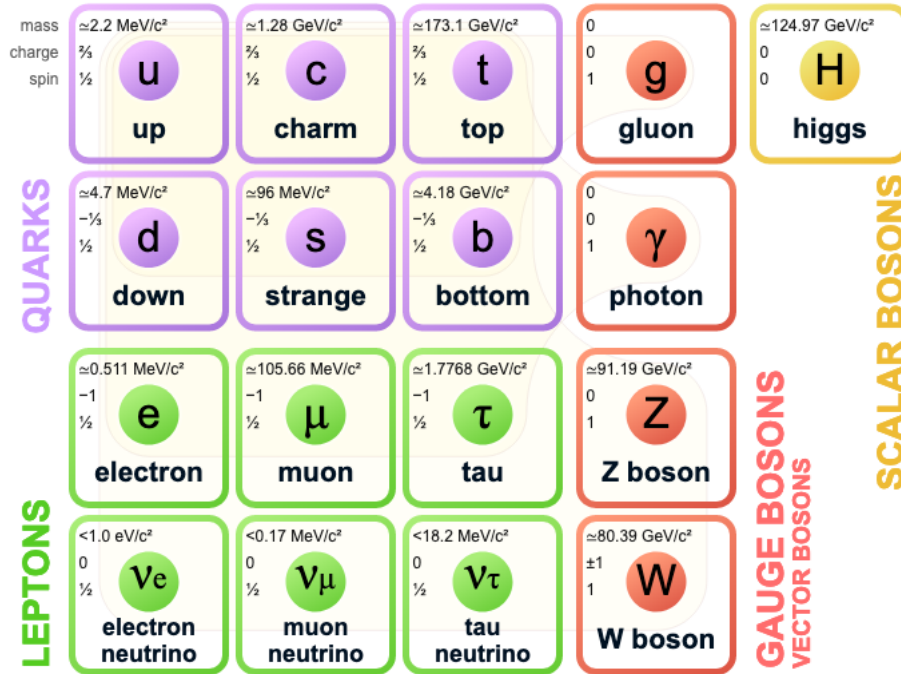
Figure 2.1: The particles described by the Standard Model. [20]

The second class of particles in the SM consists of the bosons, which have integer-valued spin. It is the exchange of these particles by which the forces propagate. Specifically, eight gluons mediate the strong force, the $W^{\pm}$ and Z^0 bosons mediate the weak force, and the singular photon mediates the electromagnetic (EM) force.

Finally, the most recently discovered particle is the Higgs Boson. This particle is a scalar or spin-0 boson, separate from the above particles which are spin-1 vector bosons. The Higgs and its associated field, are responsible for the mass of all fundamental particles. The various particles in the SM are shown in figure 2.1.

2.1.2 Gauge Symmetry

The SM presumes that all fundamental interactions are described by gauge theories. Gauge theories are quantum field theories that are invariant under a group of local transformations - the gauge transformations. The requirement of local gauge symmetry leads to the introduction of new fields - the gauge fields, whose quanta mediate the corresponding interactions.

In quantum electrodynamics (QED) the group of transformations is U(1) [17]. A U(1) gauge transformation corresponds to a change in the phase of the wavefunction, which is a function that describes quantum states in quantum mechanics. U(1) is the group of complex numbers of magnitude 1, and its transformations can be represented as multiplications by a complex exponential, the wavefunction $\Psi(x)$ is transformed as $\Psi'(x) = e^{i\theta(x)}\Psi(x)$, where $\theta(x)$ is a function of x, this is the meaning of a local transformation as opposed to a global transformation where θ would be a constant. This dependence could affect the absolute square $|\Psi(x)|^2$, violating probability conservation. To maintain gauge invariance, we introduce a gauge field, the electromagnetic four-vector potential $A_\mu(x)$ whose transformation compensates for changes in the wavefunction, preserving local gauge invariance. The gauge field $A_\mu(x)$ mediates the electromagnetic interaction, ultimately leading to photons as its quanta. Hence, the local U(1) gauge symmetry is not just a mathematical artifact but is crucial for the electromagnetic force.

For each type of interaction, there is a corresponding gauge group. The gauge group of Quantum Chromodynamics (QCD), the theory of the strong nuclear force, is SU(3). For the weak force, the gauge group is SU(2), but it can be shown that it is actually the unification of the $SU(2)_L$ weak isospin and $U(1)_Y$ weak hypercharge gauge groups that result in both the electromagnetic and weak force and that a subsequent mixing of its gauge fields is responsible for the photon and Z^0 particles.

2.1.3 Higgs Mechanism

The SM necessitates a mechanism to generate mass for particles, as experiments confirm that most particles are massive. However, the inclusion of gauge boson mass terms in the SM Lagrangian would compromise its gauge invariance. The solution to this problem is the Higgs mechanism: introducing two massive, complex scalar fields $\Phi = (\phi_1, \phi_2)$ and a potential $V = \mu^2\Phi^\dagger\Phi + \lambda\left(\Phi^\dagger\Phi\right)^2$ which has a degenerate, non-zero minimum when $\mu^2 < 0$, as shown in figure 2.2. In doing so, the electroweak gauge

The Standard Model of Particle Physics
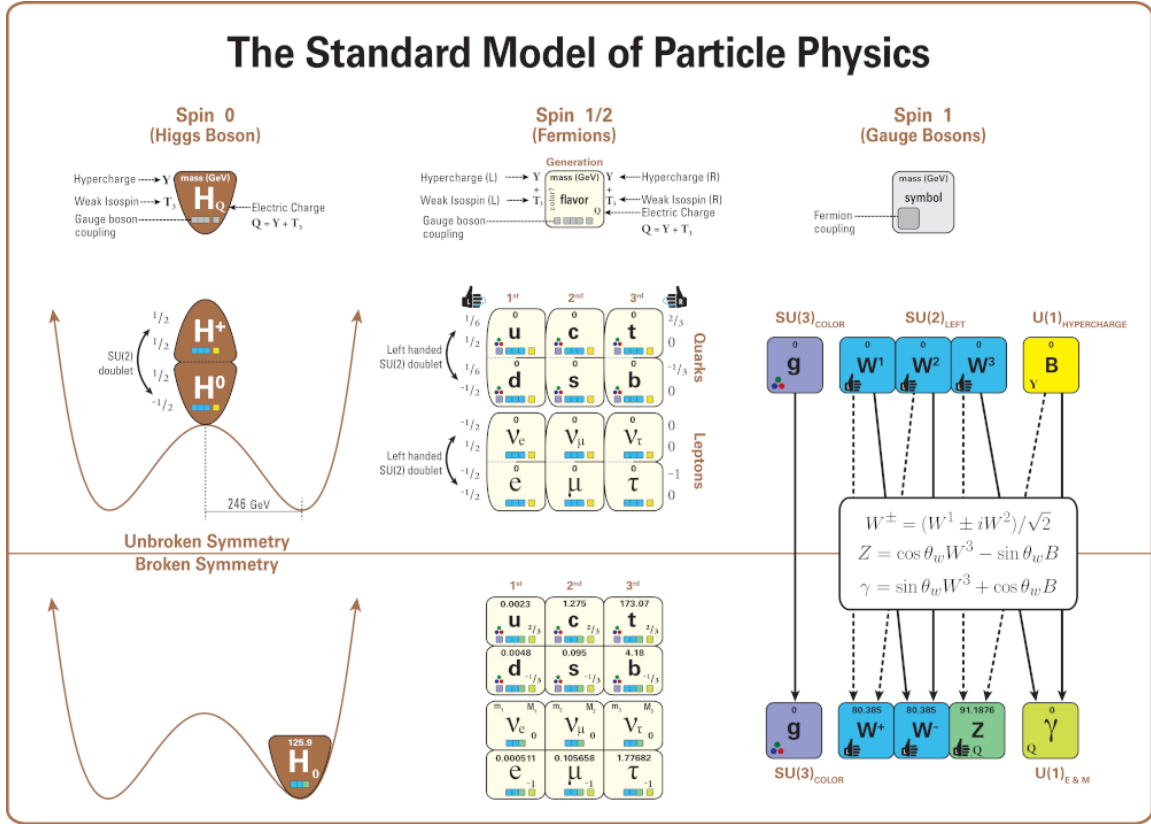
Figure 2.2: A diagram illustrating the relationship between spontaneous symmetry breaking and the particle masses. On the left, we see the shape of the Higgs potential illustrating the non-zero vacuum expectation value at the Higgs potential minimum. On the right we see the $SU(2)_L \times U(1)_Y$ W^3 and B gauge fields which give rise to the $W^\pm$, Z^0 and photon particles [21]

symmetry is broken, which provides mass to the $W^\pm$ and Z_0 bosons. Fermions then acquire mass through their couplings to the Higgs field. Figure 2.2 shows the shape of the Higgs potential and the results of the broken symmetry.

2.2 Limitations

2.2.1 Gravity

As mentioned, the SM does not describe gravity. Although some theories propose a graviton [22], a spin-2 particle that works within the quantized field theory framework, it has never been observed. The SM concerns itself with the interactions of particles on a scale in which gravity is negligible, making it inherently difficult to connect the

concepts experimentally. For reference, the coupling strength of gravity is 10^{-42} times weaker than that of strong nuclear force.

2.2.2 Higgs Naturalness

While the SM does make predictions of physical properties such as the electron magnetic moment with incredible precision [23], other important values such as almost all particle masses are parameters which must be experimentally determined [5]. The mass of the Higgs boson exemplifies this limitation. According to the SM, quantum corrections due to virtual particles should drive the mass of the Higgs boson up to the Planck scale [19], which is around 10^{19} GeV. This theoretical prediction starkly contrasts with the observed mass of the Higgs boson, which is only about 125 GeV.

This discrepancy suggests the existence of a delicate fine-tuning in the parameters of the SM, causing a cancellation that brings the Higgs mass down from the Planck scale to its observed value. However, such fine-tuning is generally considered to be 'unnatural'. From a statistical standpoint, if parameters can take a range of values, it seems implausible that they would have such a precise configuration that results in this exact cancellation unless there is a fundamental underlying mechanism.

2.2.3 Matter/Anti-Matter Asymmetry

Each particle in the SM has an anti-particle, which for charged particles is an oppositely charged particle with otherwise identical properties. There is, in principle, no reason for the universe to not contain equal parts matter and anti-matter as far as the formulation of the SM is concerned. This is in contrast with measurements that show the universe is indeed primarily made of matter [7].

2.2.4 Dark Matter

Astrophysical observations show that the rotational curves of galaxies and the dynamics of galaxy clusters are incompatible with Einsteinian gravity, and imply the

existence of dark matter [8], which does not interact electromagnetically but does interact gravitationally. The SM also does not provide a candidate identity for this matter.

2.2.5   Dark Energy

Observations dating back to the 1920s have demonstrated that the universe is in a state of expansion [24]. More recent measurements from the 1990s, particularly those involving distant supernovae, have indicated that this expansion is not merely ongoing, but is in fact accelerating [25]. To reconcile this accelerated expansion with the principles of general relativity and the gravitational attraction inherent in massive objects, a cosmological constant, denoted as Λ, is introduced [26]. This constant imparts a kind of 'negative pressure' or repulsive force to the universe. The energy associated with this cosmological constant has been termed 'dark energy', as the energy we can directly observe in the universe falls short of what would be required to account for the observed rates of expansion. However, the SM, given its exclusion of general relativity, remains silent on these cosmological phenomena and cannot offer an explanation for these observations.

2.2.6   Neutrino Oscillations

Neutrinos, elementary particles that interact primarily through the weak nuclear force, are predicted to be massless according to the SM. However, experiments observing neutrinos produced in the sun and in the atmosphere have definitively shown that neutrinos undergo oscillations between the different generations of neutrinos [27][28]. This oscillation implies that neutrinos cannot be massless.

The neutrinos produced in specific processes, such as those in the sun (electron neutrinos), do not have a definite mass. Instead, they exist in a superposition of mass states [6]. As these neutrinos propagate through space, the different mass states mix with each other, leading to a periodic change in the neutrino's flavor. This means that

an electron neutrino produced in the sun can transform into a muon or tau neutrino as it travels to Earth. When detectors on Earth measure the incoming neutrinos, they observe fewer electron neutrinos than expected but find an excess of the other flavors, confirming the oscillation process.

The discovery of neutrino oscillations has necessitated a revision of our understanding of neutrino properties and is now accepted as fact, as such, physicists hope to amend the SM to provide a comprehensive mechanism to explain neutrino oscillations.

2.3 Supersymmetry

The following description of Supersymmetry (SUSY) is a compilation of information from the following works [29][11][30]. SUSY predicts the existence of a "superpartner" for each particle in the SM. These superpartners differ from their counterparts by a spin of 1/2 [11]. This means for every fermion it is proposed there is a bosonic superpartner, and vice versa. For example, the superpartner of a quark (spin 1/2) would be a squark (spin 0), and the superpartner of a gluon (spin 1) would be a gluino (spin 1/2). The names of these superpartners are typically derived from their SM counterparts with the addition of an "s" for fermions (e.g., selectron, squark) or an "ino" for bosons (e.g., photino, gluino). In an ideal supersymmetric world, the masses of the superpartners would be identical to their SM counterparts. However, since we have not observed these superpartners in particle physics experiments, we infer that SUSY must be a broken symmetry. This means that the superpartners must be heavier than their counterparts, which is why they have not yet been detected.

2.3.1 Minimal Supersymmetric Standard Model

The Minimal Supersymmetric Standard Model (MSSM) is the simplest supersymmetric extension of the SM that remains consistent with known physical laws. It introduces a superpartner for each particle in the SM, effectively doubling the number of fundamental particles. However, the introduction of these new particles also

brings a significant increase in the number of parameters in the model. The SM has 19 free parameters, while the MSSM has over 100 [30]. These additional parameters come from the masses of the new supersymmetric particles, the mixing angles between different generations of particles, and the parameters that govern the breaking of SUSY.

One of the key features of SUSY and the MSSM is that it provides a solution to the hierarchy problem without fine-tuning [31]. The quantum corrections to the Higgs mass caused by the SM partners are counterbalanced by those of the supersymmetric partners.

SUSY predicts the existence of not just one, but five Higgs bosons [30]. In the MSSM, there are two Higgs doublets leading to five physical Higgs particles: two CP-even neutral Higgs bosons (h and H), one CP-odd neutral Higgs boson (A), and two charged Higgs bosons (H^+ and H^-). This is in contrast to the SM which predicts a single neutral Higgs boson.

2.3.2   R-Parity

R-parity is a concept introduced in supersymmetric theories to prevent rapid proton decay and to ensure the stability of the lightest supersymmetric particle (LSP) [32]. R-parity is a quantum number assigned to particles [11]:

$$R = (-1)^{3(B-L)+2S} \tag{2.1}$$

where S is the particle spin, B the baryon number, and L the lepton number. SM particles are assigned an R-parity of +1, and their superpartners are assigned an R-parity of -1. If R-parity is conserved, then superparticles can only be produced or annihilated in pairs. This implies that the LSP, if it is produced in a collider or in the early universe, cannot decay into SM particles and is therefore stable. This makes the LSP a good candidate for dark matter [13], as it would not have decayed away over the history of the universe.

2.3.3 Minimal Supergravity - mSUGRA

Minimal Supergravity (mSUGRA) extends the principle of SUSY to include gravity and is well described in [12][33][34], which this section briefly summarizes. It is a specific version of the MSSM where the gravitational force is mediated by a spin-2 particle called the graviton and its supersymmetric partner, the spin-3/2 gravitino. The inclusion of gravity in the theory leads to the concept of grand unification, as it provides a framework in which all four fundamental forces—gravity, electromagnetism, the weak force, and the strong force—can be described within a single theoretical structure.

In the Minimal Supergravity (mSUGRA) model, at the grand unification scale, the parameters associated with the breaking of SUSY (referred to as "soft" SUSY breaking terms) take on universal values. This concept, known as "universality," implies that all scalar superpartners of fermions (squarks and sleptons) and all fermionic superpartners of gauge and Higgs bosons (gauginos and higgsinos) have the same mass at the grand unification scale. The assumption of universality in mSUGRA simplifies the model by reducing the number of independent parameters, making it more tractable for theoretical and experimental study.

In the mSUGRA framework, additional assumptions are made to reduce the number of free parameters in the model; the supersymmetric sector of the theory is described by just five parameters:

1. The universal scalar mass, m_0, which is the mass of the scalar superpartners at the grand unification scale.

2. The universal gaugino mass, $M_{1/2}$, which is the mass of the fermionic superpartners at the grand unification scale.

3. The universal trilinear coupling, A_0, which determines the strength of the interactions between the scalar particles.

4. The ratio of the vacuum expectation values of the two Higgs doublets, $\tan \beta$.

11

5. The sign of the Higgsino mass parameter, $\text{sgn}\,(\mu)$.

2.3.4 Renormalization Group Equations

The mSUGRA parameters are defined at the grand unification scale. However, the properties we observe in particle physics experiments, such as particle masses and decay rates, are defined at the electroweak scale, which is much lower.

The connection between these high-scale parameters and the low-scale observables is provided by the renormalization group equations (RGEs). This complex topic is covered in detail in [11][29], and briefly summarized here. The RGEs are a set of differential equations that describe how the parameters of a quantum field theory change with the energy scale. In the context of SUSY, they describe how the soft SUSY-breaking parameters evolve from the grand unification scale down to the electroweak scale.

When a specific set of mSUGRA parameters is chosen, the RGEs can be numerically solved to predict the masses of the supersymmetric particles, their couplings, and other properties at the electroweak scale. This includes the masses of the squarks, sleptons, gauginos, and Higgs bosons, as well as the elements of the mixing matrices in the quark and lepton sectors. The RGEs also predict the couplings that determine the decay rates of the supersymmetric particles. For instance, the lifetime of a supersymmetric particle is inversely proportional to the square of its coupling to the particles it decays into.

2.3.5 Long-Lived Charged Particles

In the framework of mSUGRA, the lightest supersymmetric particle (LSP) is often taken to be a neutralino or a slepton. However, there are regions within the mSUGRA parameter space where the gravitino can be the LSP, this model and its consequences are described in [12][35][36] and used throughout this thesis. In this model, if R-parity is conserved, a principle often assumed in supersymmetric theories, as explained in

2.3.2, the gravitino becomes stable. It is this parameter space, where the values $m_0 = A_0 = 0$, $\tan \beta = 10$, $sgn\,(\mu) > 0$, and the value of $M_{1/2}$ is in a range from $300 - 1300$ GeV, that is explored in this thesis.

The gravitino only interacts gravitationally, leading to interactions that are suppressed by the Planck scale. This suppression has significant implications for the decay of the next-to-lightest supersymmetric particle (NLSP) into the LSP. If the NLSP is a stau, the supersymmetric partner of the tau lepton, its decay into a tau lepton and a gravitino is also Planck-suppressed. The lifetime of the stau, denoted by τ, can be expressed in terms of the stau mass $(m_{\tilde{\tau}})$, the gravitino mass $(m_{\tilde{G}})$, and the Planck mass (M_*) [12].

$$\tau = \frac{\hbar}{\Gamma}, \quad \text{with}$$

$$\Gamma\left(\tilde{\tau} \to \tau \tilde{G}\right) = \frac{c^2}{48\pi M_*^2} \frac{m_{\tilde{\tau}}^5}{m_{\tilde{G}}^2} \left(1 - \frac{m_{\tilde{G}}^2}{m_{\tilde{\tau}}^2}\right)^4 \tag{2.2}$$

Additionally, mSUGRA theories predict the gravitino mass as

$$m_{\tilde{G}} = \frac{1}{c^2} \frac{F}{\sqrt{3} M_*} \tag{2.3}$$

Where $\sqrt{F}$ is the SUSY breaking scale.

In this scenario, the stau always decays into a tau lepton and a gravitino. Because the stau's lifetime depends solely on the masses of the stau, the gravitino, and the Planck mass, and given the relation of the gravitino to the SUSY breaking scale in 2.3, which is an open parameter, we can choose the stau lifetime, setting the gravitino mass and SUSY breaking scale. If the superpartner mass scale is on the order of 100 GeV, the gravitino mass is also on this scale and the lifetime of the stau naturally falls within the range of approximately 10^4 seconds to 10^8 seconds.

2.3.6 Cosmological Motivation

The study of SUSY and SUSY breaking can take on a myriad of forms, requiring justification for the specific SUSY model under consideration. As in the previous

section, references [12][35][36] as well as [37] motivate the physics case for the parameters discussed here. The mSUGRA model with a gravitino LSP and stau NLSP is particularly interesting for several reasons. The gravitino, due to its gravitational interactions, is a superweakly interacting massive particle (superWIMP), making it an excellent dark matter candidate. If the gravitino is not the LSP, its late decays would require reheating temperatures that contradict requirements set by thermal leptogenesis [36].

Scenarios with a neutralino NLSP are possible but can lead to excess hadronic energy in the early universe, conflicting with the successes of big bang nucleosynthesis (BBN), unless some mechanism can highly suppress these decays.

Furthermore, while the stau lifetime naturally falls within the range of 10^4 seconds to 10^8 seconds, constraints from the cosmic microwave background (CMB) and BBN place an upper limit on the stau lifetime of roughly one year [12][35][36]. However, NLSP decays that occur late enough to have their decay products thermalize according to the CMB and BBN constraints may be able to destroy ^{7}Li, bringing the predicted levels of ^{7}Li in the universe down to observed levels, conveniently solving a major open problem in cosmology [36]. Thus, a stau with a lifetime of approximately 1 month is a favourable choice for the NLSP. With these factors in mind, stau lifetimes of 7, 30, 90, 150, and 365 days are studied in this thesis.

Chapter 3

Experimental Apparatus

3.1   The LHC

The following chapter is a compilation of information primarily found in [1][38] as well as the ATLAS technical design reports [39–48], the CERN public website, as well as other sources where noted.

The LHC is a 27 km two-ring-superconducting-hadron collider about 100 meters beneath the earth's surface, located at the Franco-Swiss border near Geneva, Switzerland, at the European Organization for Nuclear Research (CERN), the geographic layout is shown in figure 3.1. The tunnel, constructed between 1984 and 1989, which houses it was originally built for the Large Electron Positron collider (LEP). The purpose of the accelerator is to propel proton beams to a center of mass energy level of $\sqrt{s} = 14$ TeV [38]. Since its initial construction, the LHC has undergone several upgrades and at the time of thesis operates at a center of mass energy of $\sqrt{s} = 13.6$ TeV [49].

The LHC operates in a cycle of active runs and long shutdowns. During a run, protons are continuously accelerated and brought into collisions to generate data for a variety of physics experiments. During a long shutdown, the LHC is non-operational, allowing for maintenance, repairs, and upgrades of the detectors and accelerating devices.

The proton beams are accelerated in opposite directions within the LHC tunnel
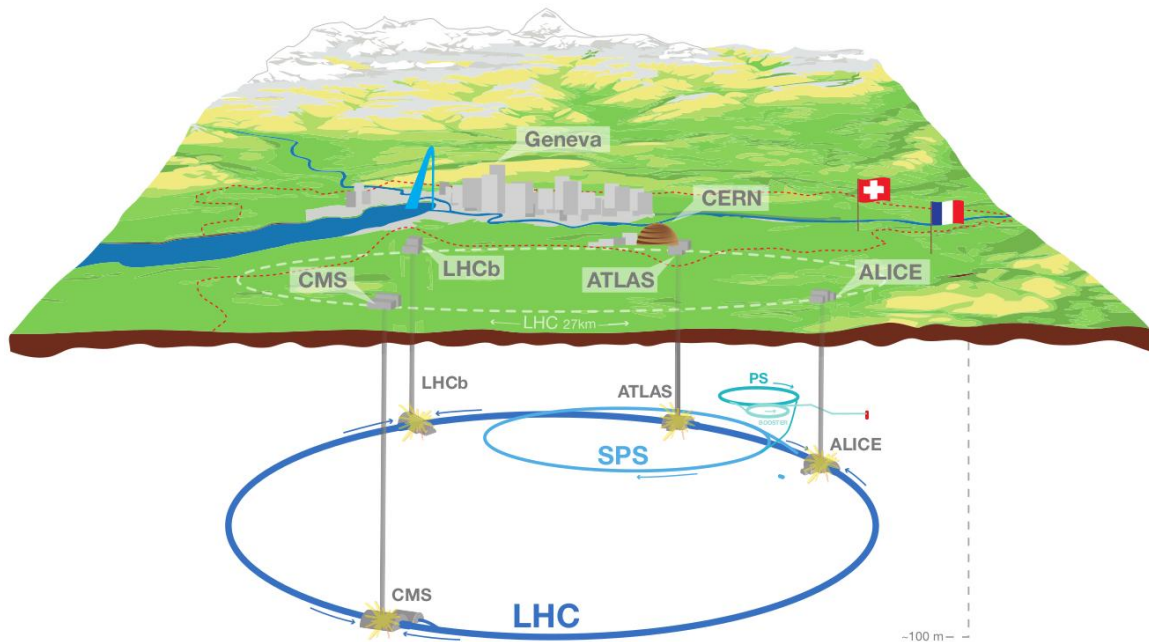
Figure 3.1: An illustration showing the 27 km LHC rings and orientation with respect to the local geography [50].

and then steered into collision at four distinct interaction points. These points host the four main LHC experiments: ATLAS and CMS, the two largest multi-purpose experiments; LHCb, focused on precision measurements of CP violation and rare decays of hadrons; and ALICE, dedicated to studying the properties of quark-gluon plasma produced in heavy ions collisions, which the LHC is also capable of producing. In addition to these four main experiments are five complementary experiments: MoEDAL-MAPP [51][52], TOTEM [53], FASER [54], LHCf [55], and SND [56].

The accelerator complex of the LHC begins with the injection chain. The protons used in collisions originate from hydrogen gas [57], which is stripped of its electrons and fed into the linear accelerator called Linac4. This first step accelerates the protons to an energy of 160 MeV. The protons are then transferred to the Proton Synchrotron Booster (PSB), where their energy is increased to 2 GeV. The protons are then injected into the Proton Synchrotron (PS) and further accelerated to 14-26 GeV. The final stage of the injection chain, the Super Proton Synchrotron (SPS), brings the protons up to an energy of 450 GeV, at which point they are ready to be injected

16
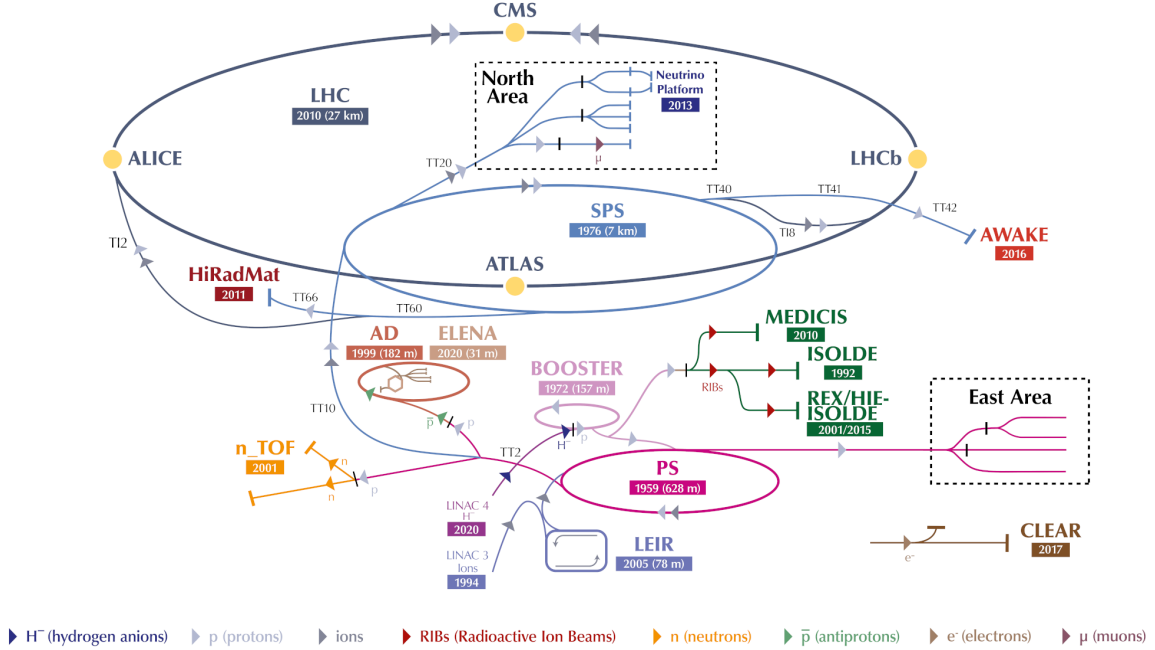
Figure 3.2: A diagram of the LHC accelerator complex [60].

into the main LHC ring [58] [59]. A diagram of the LHC complex and its many components is shown in figure 3.2.

To facilitate acceleration from 450 GeV to 7 TeV, the LHC uses Radio Frequency (RF) cavities and bending magnets. The RF cavities provide longitudinal acceleration necessary to increase the beam energy, while the bending magnets ensure transverse acceleration to maintain the particles in a circular trajectory. The LHC uses 1232 superconducting dipole magnets consisting of coils of superconducting Niobium-Titanium (NbTi) cooled down to 1.9 K by superfluid helium to generate a magnetic field of 8.33 T. These magnets maintain the protons in orbit at the design energy level of 7 TeV. Quadrupole magnets are used to focus the beams of the accelerator. [61][62]

The LHC's cooling system is responsible for maintaining this ultra-low temperature. To achieve this, an extensive cryogenic system, using both liquid nitrogen and superfluid helium, is employed.

The LHC ring is divided into eight sections or "points". At Points 1, 2, 5, and

8, the counter-rotating beams are brought together to yield collisions. These are the interaction points that house the main experiments. The remaining points accommodate various beam service facilities, including the beam cleaning services at Points 3 and 7, which collimate the beams to prevent particles from straying from the main beam path. The superconducting RF cavities, used to increase the energy of the beam from 450 GeV to 7 TeV, are located at Point 4. At Point 6, the "beam dump" facility uses "kicker" magnets to quickly redirect the beams out of the LHC ring and into an external absorber in case of malfunctions.

3.1.1 Beam Structure

The LHC employs a sophisticated process for proton beam circulation. Contrary to what one might imagine, the protons do not form a continuous flow. They are, instead, batched into groups known as "bunches". These bunches are initially organized by the smaller machinery within the LHC's injection chain, and their final structure is maintained by the RF cavities.

The RF cavities generate an oscillating electromagnetic field that acts longitudinally, causing the bunches, each composed of approximately 10^{11} protons, to undergo what is called synchrotron oscillations around the central node of the RF oscillation. This phenomenon happens while the bunches make their rounds through the LHC ring. The oscillating RF field then moulds the proton bunches. If protons are lagging or are ahead of the ones at the bunch's center, they are either accelerated or decelerated to reposition them into the bunch's center. Figure 3.3 illustrates the shape and position of the bunches relative to the RF waveform.

The LHC RF cavities operate at a frequency of 400 MHz, which sets the proton bunch placements. These placements are termed "RF buckets", and combined with the LHC's circumference, determine the maximum number of proton bunches that can be accommodated in the LHC. With the LHC operational, there are approximately 35640 RF buckets available, although not all are filled with proton bunches.
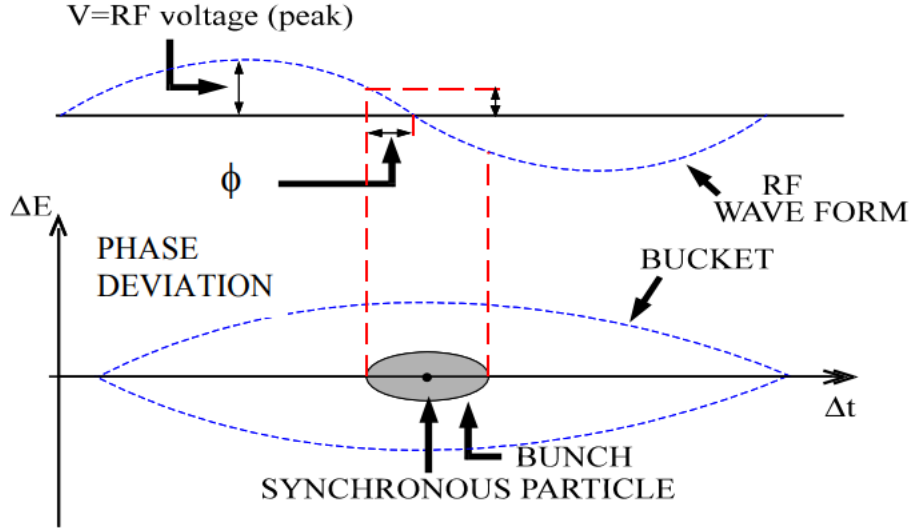
Figure 3.3: Illustration of the RF bunching of protons in the LHC beam. The RF voltage determines the phase deviation of the beam and therefore the structure of the bunch. [63]

Additionally, during normal operations, as bunches are collided at the interaction points the train of "buckets" decays and is periodically refilled.

The minimum separation between RF buckets containing proton bunches is 10 RF buckets, implying a gap of at least 9 unfilled RF buckets following one containing a proton bunch. This equates to a minimal 25 nanoseconds inter-bunch duration, also known as "bunch spacing". As of the present time, the LHC operating conditions during run 3 are expected to reach 2808 bunches spaced 25 ns apart, with 1.8×10^{11} protons per bunch (ppb) [49]. The LHC operators and the capabilities of detectors at points 1, 2, 5, and 8 dictate the bunch spacing and overall bunch structure. This is because shorter bunch spacing translates to a higher intensity and multiplicity of collisions at these interaction points. A 25 ns bunch spacing equates to a maximum pp collision rate of 40 MHz, a limit defined by the design of the detectors at these interaction points.

There may be instances where issues occur during the LHC filling process, which can lead to bunches occupying incorrect RF buckets. This, in turn, can cause collisions to happen at the wrong places within the detectors, disrupting their data acquisition

systems. If the beam quality is unsatisfactory, the beam is dumped, and the LHC is refilled. The beam dumping process involves the use of kicker magnets to divert the beam out of the storage ring. The kicker magnets need at least a 3 μs window to ramp up the magnet currents. Hence, all filling schemes need to incorporate a lengthy abort gap to allow the kicker magnets to attain full field strength. The refilling process of the LHC takes about 3 minutes per beam [64].

3.1.2   Luminosity

Luminosity, in the context of high-energy physics and the LHC, is a measure of the number of potential collisions that can occur. The higher the luminosity, the more collisions there are, and hence the more data we can acquire. Instantaneous luminosity, as the name suggests, refers to the luminosity at a given instant in time, and is a function of the beam shape, and population, given by [65]:

$$\mathcal{L} = \gamma \frac{n_b N_p^2 f_{rev}}{4\pi \beta^* \varepsilon_n} R, \quad R = 1/\sqrt{1 + \frac{\theta_c \sigma_z}{2\sigma_{xy}}} \tag{3.1}$$

Here γ is the proton beam energy in units of rest mass, $n_b = 2808$ is the number of bunches, $N_p = 1.8 \times 10^{11}$ the bunch population, and f_{rev} the revolution frequency. β^*, ε_n, θ_c, σ_z, and σ_{xy} are all geometrical factors that describe the shape of the beam. More specifically, the focal length, normalized transverse emittance, crossing angle, transverse, and longitudinal r.m.s size, respectively. We can see that the luminosity depends quadratically on the bunch population but only linearly on the number of bunches. The instantaneous luminosity is not held constant during accelerator experiments, over time the beam decays, distorts, and must be refilled; this is in addition to any unexpected technical issues that might arise. Therefore the integrated luminosity is used as a measure of the total number of collisions achieved.

$$L_{int} = \int \mathcal{L} dt \tag{3.2}$$

Then, the number of events of a given quantum process is given by the product of the integrated luminosity and the cross section σ for that process

$$N = L_{int} \cdot \sigma \tag{3.3}$$

3.1.3   High Luminosity LHC

The LHC started its research activities in the spring of 2009. As of the present moment, the LHC has completed two runs; Run 1 from 2009 to 2012 and Run 2 from 2015 to 2018. During Run 1, the collider was set to operate at center-of-mass energies of 7 TeV and 8 TeV with a bunch spacing of 50 ns. It yielded 5.61 fb^{-1} of 7 TeV data and 23.3 fb^{-1} of 8 TeV data in 2011 and 2012, respectively. In the course of Run 2, the LHC was set to function at a center-of-mass energy of 13 TeV and a bunch spacing of 25 ns. Owing to the heightened instantaneous luminosity, 156 fb^{-1} of data was collected during these years. [66]

The LHC has, at the time of this writing, initiated Run 3, which is projected to continue until the close of 2025. A minor increase in center-of-mass energy to 13.6 TeV has been made, while the integrated luminosity is expected to be double that delivered so far. This is achieved by changing beam parameters such as the bunch population and beam emittance as seen in 3.1 [49]. Following Run 3, the benefits of operating the accelerator without a substantial increase in luminosity will become minimal. Consequently, to ensure the continuity of scientific advancement, the LHC will undergo an upgrade to operate at 14 TeV and up to 10 times higher instantaneous luminosity, with an expected accumulated dataset of approximately 3000 fb^{-1} by 2039 [67]. This initiative is known as the High Luminosity LHC (HL-LHC) and is anticipated to commence operations in 2029. The HL-LHC is expected to deliver about 715 fb^{-1} of data during its fourth run [68], which is the period explored in this research.
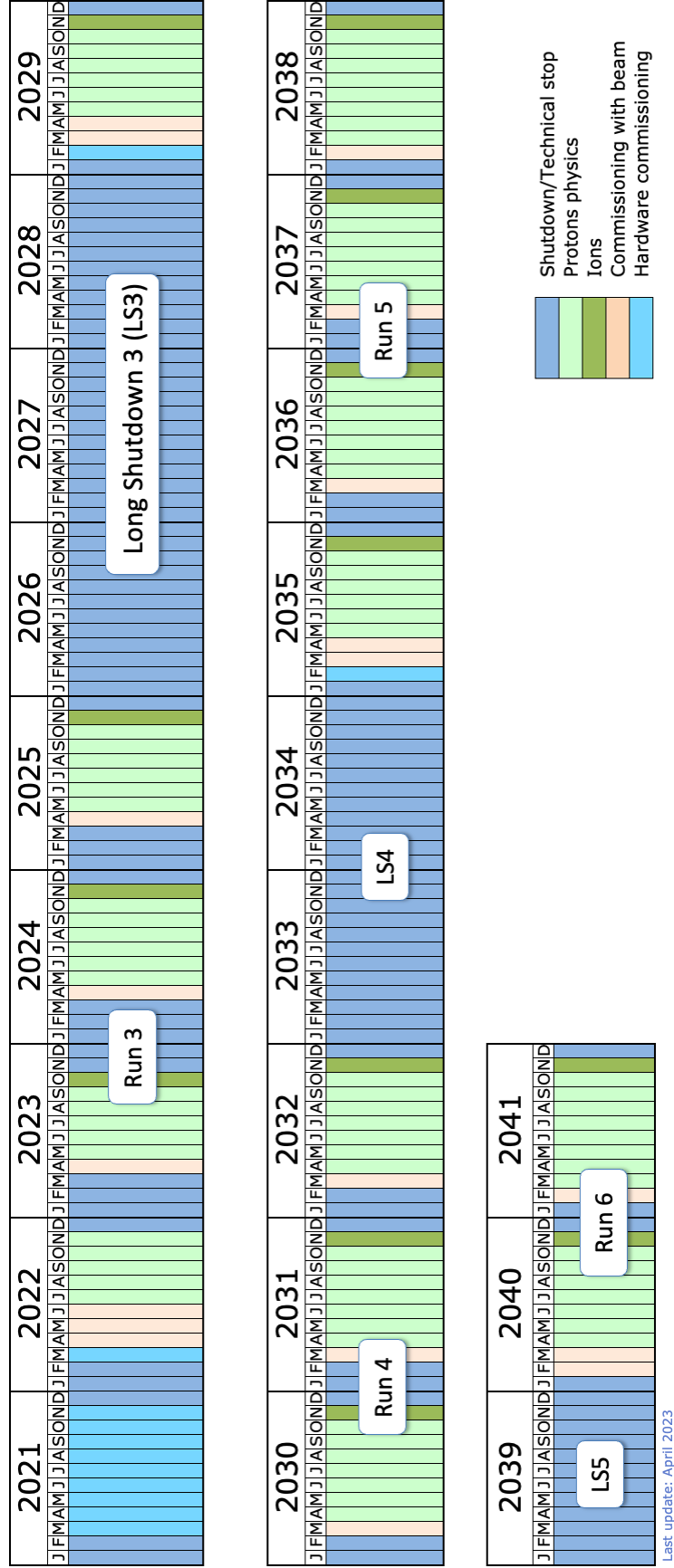
Figure 3.4: The projected operating schedule of the LHC. There are expected to be 27 months of proton-proton physics during run 4.

3.2 The ATLAS Experiment

ATLAS (A Toroidal LHC ApparatuS) is a general-purpose detector, situated approximately 100m below ground at Point 1 on the LHC ring. The detector is cylindrically symmetric around the beam axis, as well as forward-backward symmetric with respect to the interaction point, effectively covering nearly the full 4π solid angle around the interaction point. At an impressive scale of 44m in length, 25m in diameter, and a total mass of about 7000 tons, ATLAS stands as one of the most complex and extensive scientific experiments ever constructed [1].

The detector structure consists of concentric cylindrical sub-detectors, which envelop the interaction point (IP). These sub-detectors are layered about the interaction point and extend into two end-cap structures where the detector layers form disks. The design reflects the fact that the proton-proton (pp) interactions in the LHC have no preferred direction in the plane transverse to the beamline, thereby making it necessary for the detector to cover all possible directions of particle flight.

The innermost part of the detector, the Inner Detector (ID), is responsible for reconstructing the trajectories of charged particles and locating them with respect to the interaction point. Encased in a 2 T axial magnetic field from a solenoid magnet that surrounds it, the ID measures the momentum of these particles by observing the bending of their tracks in the magnetic field. The ID features a silicon pixel detector, a semiconductor microstrip detector, and a straw-tube tracker capable of detecting electron transition radiation.

Outside the solenoid lies the calorimeter system, composed of an electromagnetic subsystem (ECAL) and a hadronic subsystem (HCAL). The ECAL is designed for the identification of electromagnetic showers, while the HCAL performs energy measurements of jets and missing transverse momentum.

The outermost subdetector, the Muon Spectrometer (MS), identifies muons and measures their momentum. This system is installed inside and around a set of toroidal

magnets, providing a precise muon momentum measurement. Additionally, the AT-LAS detector contains subdetectors that are designed specifically for the measurement of luminosity.

Data acquisition, including triggering mechanisms, are integral parts of the ATLAS infrastructure. The detector subsystems are designed to withstand high-intensity radiation doses from the LHC, employing fast, radiation-hard, or shielded electronics capable of providing distinct readouts for a 25 ns bunch-crossing rate. However, due to the enormity of data produced, a selective trigger system is required to filter the most interesting events for further offline analysis.

3.2.1 Coordinate System

The ATLAS experiment uses a specific coordinate system to accurately describe the positions and directions within the detector. The coordinate system is based on a right-handed Cartesian system with the origin at the interaction point in the center of the detector.

The axes are defined as follows: the x-axis points towards the center of the LHC ring, the y-axis points upwards, away from the center of the earth, and the z-axis points along the beam axis, in the counter-clockwise direction when viewed from above. This Cartesian system is also converted into a polar coordinate system with radial distance z still pointing in the direction of the beam pipe, the polar angle θ which points along the positive z axis when $\theta = 0$, and the azimuthal angle ϕ which rotates through the x-y plane and is along the positive x axis when $\phi = 0$.

To describe the motion of particles within the detector, a few other measures are commonly used, the pseudorapidity (η) and the rapidity (y).

$$y = \frac{1}{2} \ln \left(\frac{E + p_z}{E - p_z} \right) \tag{3.4}$$

Where E is the energy of the particle and p_z is the longitudinal momentum. This is a Lorentz-invariant quantity under boosts along the beam direction, and a difference

in rapidity gives an invariant measure for such boosts. Its convenience is also due to the fact that it can be calculated from geometric quantities without knowing any particle properties.

Pseudorapidity is often preferred over the polar angle θ as the particle flow is approximately uniform per unit in η [69]. It is defined as:

$$\eta = -\ln\left(\tan\left(\theta/2\right)\right) \tag{3.5}$$

For ultra-relativistic particles (particles moving very close to the speed of light), where the mass rest energy is negligible relative to the total energy, the pseudorapidity coincides with the rapidity. For reference, ATLAS has a coverage of $|\eta| < 4.9$.

Another measure often used is the angular distance in pseudorapidity-azimuthal angle space, defined as $\Delta R = \sqrt{\Delta\eta^2 + \Delta\phi^2}$, which helps to quantify the angular separation between two objects.

Transverse quantities such as the transverse momentum (p_T), transverse energy (E_T), and missing transverse energy (E_{Tmiss}) refer to the projections of these quantities onto the x-y plane, perpendicular to the beam direction.

3.2.2 Magnet System

The ATLAS experiment is equipped with a complex magnet system that facilitates the detection and analysis of charged particles. The system is maintained at an operating temperature of approximately 4.5 Kelvin. By means of the Lorentz force, charged particles will travel along a curved path within a magnetic field. The curvature of this path varies with the particle's momentum and the strength of the applied magnetic field. This fundamental relationship is exploited by ATLAS to provide accurate momentum measurements of the particles produced.

Mathematically, the relationship is expressed as:

$$p_T = qBr \tag{3.6}$$

Here, p_T represents the transverse momentum of the particle, q is the charge of the particle, B is the magnetic field, and r is the bending radius.

The ATLAS magnet system, shown in figure 3.5 comprises four superconducting magnets: an inner solenoid, a barrel toroid, and two end-cap toroids, all of which are cooled with liquid helium [39].

The inner solenoid magnet encloses the inner detector (ID) and produces a 2 Tesla (T) axial magnetic field. This field influences the trajectories of charged particles to curve within the transverse (x-y) plane. The solenoid is designed to minimally interfere with particles, ensuring high-resolution energy measurements in the calorimeters. Constructed from superconducting wire, the solenoid shares a vacuum chamber with the electromagnetic calorimeter to avoid adding additional material. The solenoid extends 5.8 meters along the z-axis, covering a diameter of 2.56 meters, with a thickness of 4.5 centimetres.

The toroid magnet system is divided into two main sections like much of the inner sections, a barrel region and an end-cap region to cover different regions of pseudorapidity (η). The large barrel toroid covers the range $|\eta| < 1.4$, while the end-cap toroid systems handle the range $1.6 < |\eta| < 2.7$. The magnet system offers an average field of 4 Tesla, maintaining a nearly constant bending strength across the ranges, excluding the transitional region between the barrel and end-cap toroids ($1.6 < |\eta| < 2.7$).

The barrel toroid magnet and the two end-cap toroids are part of the outermost layer of ATLAS, the muon spectrometer, and are equipped with eight evenly spaced superconducting coils. These create an azimuthal magnetic field, which influences the muons' trajectories to bend within the transverse and z directions. The magnetic field within these toroids varies, exhibiting a complex structure. In the barrel, the peak field is 3.9 T, while in the end-cap toroids, the peak field is 4.1 T. The barrel toroid magnet system measures 9.4 meters in inner diameter and 20.1 meters in outer diameter, spanning 25.3 meters along the beam direction, making it the largest toroidal magnet ever produced.
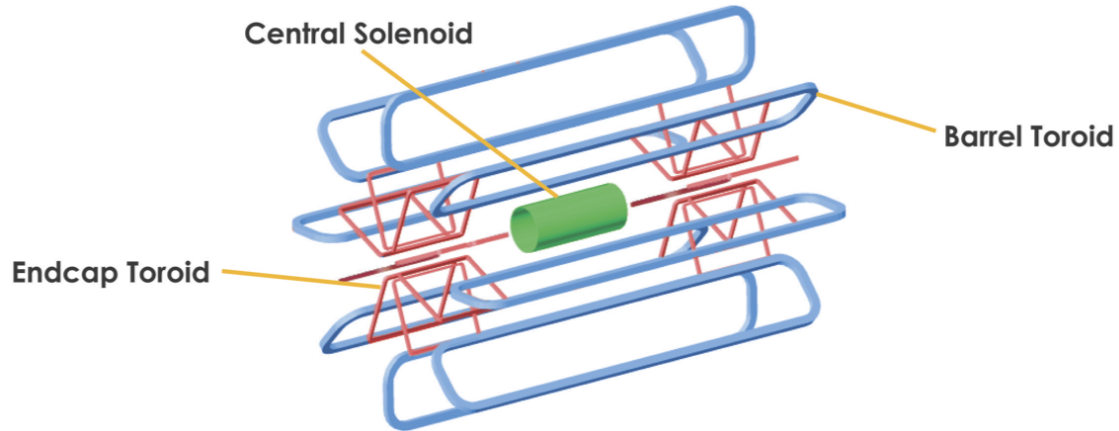
Figure 3.5: A diagram that shows the magnet systems contained in the ATLAS experiment. [39]

Field sensors map the complex structure of the magnetic field. These precise mappings are crucial for the accurate measurement and analysis of the particles' paths and momenta.

3.2.3 Inner Detector

The Inner Detector (ID) of the ATLAS experiment, the component closest to the collision point, is designed for the tracking and measurement of charged particles. Its momentum resolution is critical for both primary and secondary vertex identification. The ID is housed within a cylindrical envelope with a length of 7.02 m and a radius of 1.15 m. It's composed of three independent and complementary sub-detectors: the Pixel Detector, the Semiconductor Tracker (SCT), and the Transition Radiation Tracker (TRT) [44], which are illustrated in figures 3.6 and 3.7.

The Pixel Detector is the closest component to the LHC beam line, situated at just 3.3 cm. It comprises four layers of silicon pixels, each smaller than a grain of sand. When charged particles emerge from the collision point, they deposit small amounts of energy in the Pixel Detector. These signals are measured with a precision of nearly 10 μm, providing data on the origin and momentum of the particles. The compact Pixel Detector houses over 92 million pixels and almost 2000 detector elements within
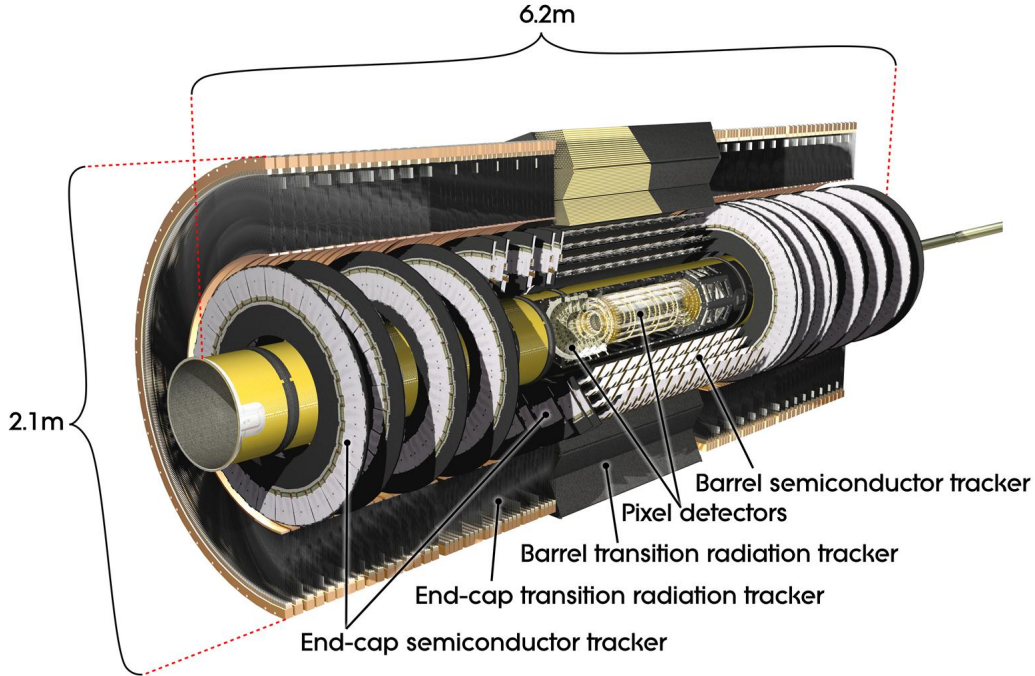
Figure 3.6: A computer generated image of the ATLAS inner detector system

an area of approximately 1.9 m^2, consuming around 15 kW of power. The pixel size is 50 x 400 μm^2 for the external layers and 50 x 250 μm^2 for the innermost layer (IBL). The Pixel Detector is structured with four barrel layers consisting of 1736 sensor modules, and three disks in each end-cap, with 288 modules.

Surrounding the Pixel Detector is the Semiconductor Tracker (SCT), employed to detect and reconstruct the tracks of charged particles produced during collisions. The SCT is composed of more than 4000 modules, containing 6 million "micro-strips" of silicon sensors. It is designed such that each particle crosses at least four layers of silicon, enabling a precision of up to 25 μm in measuring particle tracks. The SCT includes 4,088 two-sided modules and over 6 million implanted readout strips distributed over 4 cylindrical barrel layers and 18 planar end-cap discs.

The third component of the ID is the Transition Radiation Tracker (TRT). Unlike the two previous sub-detectors, the TRT consists of 300,000 thin-walled drift tubes, or "straws". Each straw, with a diameter of 4 mm, contains a 30 μm gold-plated

tungsten wire at its center. The straws have a strong electric field applied within them and are filled with a gas mixture, which gets ionized when charged particles pass through them, causing electrons to drift toward the wire, inducing an electric signal. The TRT features 350,000 read-out channels within a 12m^3 volume. Precision measurements of 0.17 mm are achieved by relating the particle drift time to the wire.

In addition to the gas mixture used inside the straw tubes, the TRT uses materials outside the straws that cause transition radiation to occur when particles pass through. The transition radiation is in the form of X-rays and the amount is dependent on the Lorentz gamma term $\gamma = E/m$, allowing for particle identification because of the mass term.

The inner detector TRT consists of a barrel region that covers a pseudorapidity range from $1.0 < |\eta| < 2.0$ with 1.5m straws that lay parallel to the beam pipe, as well as 2 end-caps covering pseudorapidity $|\eta| < 1.0$ with 0.4m straws perpendicular to the beam pipe.

3.2.4 Calorimetry

The ATLAS detector includes a series of calorimeters designed to measure the energy of particles as they pass through the detector. Calorimeters absorb most of the particles coming from a collision, forcing them to deposit their energy and halt within the detector. The calorimeters in the ATLAS detector include both electromagnetic and hadronic calorimeters, each of which has a barrel and end-cap region. Figure 3.9 shows the layout of the various calorimeter sections.

The ATLAS electromagnetic calorimeter (ECAL) is contained in the Liquid Argon calorimeter (LAr) and surrounds the ATLAS Inner Detector. The barrel and end-cap regions of the electromagnetic calorimeter feature layers of lead that absorb incoming particles, transforming them into a "shower" of lower energy particles. These secondary particles then ionize the liquid argon sandwiched between the layers, generating charges. An electric field is applied within the ECAL, causing the generated
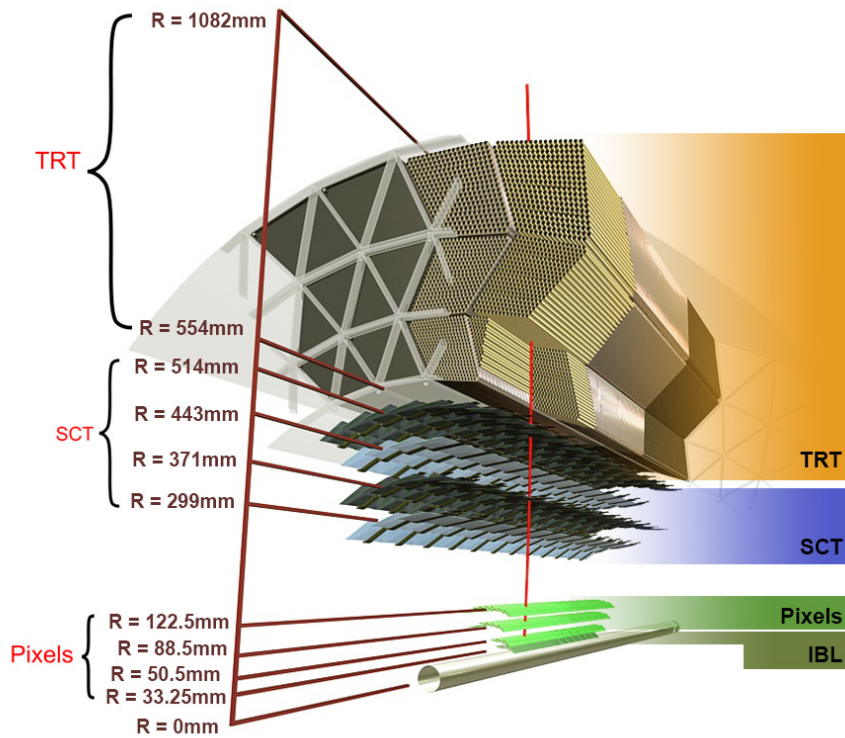
Figure 3.7: A cutaway view of the 3 main regions of the inner detector. [70]

charges to drift towards an anode, where the charge is collected and transformed into an electric current. The detected currents are summed to determine the energy of the initial particle that hit the detector. The structure features several alternating layers of these materials in a distinct accordion geometry, shown in figure 3.8, to reduce azimuthal cracks that particles could pass through without interacting [71].

Electrons and photons entering the electromagnetic calorimeter initially lose energy via pair production and bremsstrahlung until they no longer have enough energy to initiate these processes at which point other interactions such as ionization and excitation take over. The objective of the electromagnetic calorimeter is to measure the intensity of EM showers produced in the liquid argon while eventually stopping the primary particles via the dense lead. As such, electromagnetic calorimeters are often described in terms of their radiation length (X_0), a material property which is defined as the distance which a particle must travel through a material to lose $1/e$ 37%
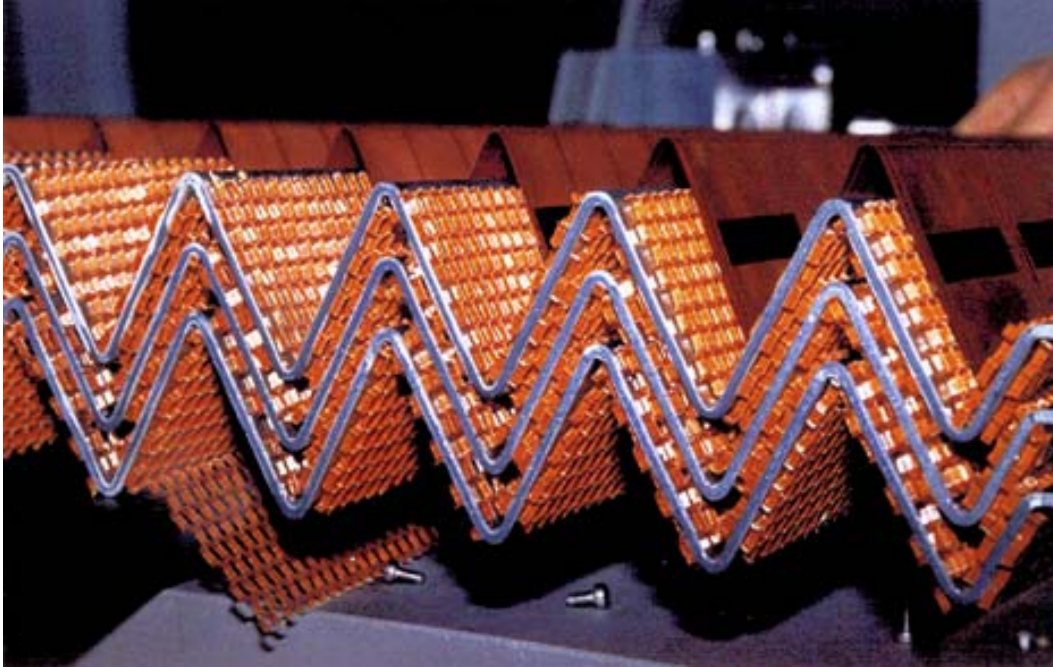
Figure 3.8: An image of the accordion patterned layers of copper-clad lead inside the electromagnetic calorimeter. [71]

of its initial energy. The electromagnetic calorimeter's thickness in units of radiation length is 24 and 26 X_0 in the barrel and end cap regions, respectively. In geometric terms, the transverse radius of the electromagnetic calorimeter barrel and end-cap covers the region 1.15-2.25m from the interaction point [46]

Particle showers are produced in the hadronic calorimeters, like in their electronic counterparts, but undergo more complex processes due to strong force interactions with the material's nuclei. Interactions such as spallation, nuclei de-excitations, intranuclear cascades, and neutron capture, can produce electromagnetic secondaries in the form of gamma rays, but also non-electromagnetic showers when nucleons (jets), or smaller nuclei are ejected. The proportions of energy deposited into these different fractions are not consistent, and some cannot be measured, therefore hadronic calorimeters require careful calibration [72].

Hadronic calorimeters are characterized by a nuclear interaction length λ_{int}. This is the mean length a hadron may travel before interacting with a nucleus in the material

31

it is traversing. This length may be several times larger than the radiation length, this allows for differentiation between electrons and hadrons but requires hadronic calorimeters to be larger in size. The thickness of the different hadronic calorimeter elements have thickness in units of interaction lengths of between 9-12λ_{int} [46][47].

The liquid argon calorimeter also contains part of the hadronic calorimeter. After the accordion structure of the electromagnetic calorimeter in the end-cap region, there are conventional planar layers of copper and liquid argon, which work by the same principle as the ECAL, and form the hadronic end-cap.

The final section of the liquid argon calorimeter is the forward calorimeter. This section is nested within the inner radius of the end-caps and surrounds the beam pipe, the region that sees the most intense particle flux, and with this in mind is designed for radiation hardness. Similar to the hadronic end-cap it features copper and argon layers but also includes additional tungsten argon layers.

In terms of dimensions, the LAr calorimeter barrel is 6.4m long and 53cm thick with 110,000 channels. The LAr end-cap includes the forward calorimeter, electromagnetic (EM) and hadronic end-caps. EM end-caps each have a thickness of 0.632m and radius of 2.077m, while the hadronic end-caps consist of two wheels with thicknesses of 0.8m and 1.0m and a radius of 2.09m. The forward calorimeter consists of three modules each with a radius of 0.455m and thickness of 0.450m.

The Tile Hadronic Calorimeter surrounds the LAr calorimeter, measuring the energy of hadronic particles which do not deposit all their energy in the LAr Calorimeter. It comprises layers of iron (steel) and plastic scintillating tiles. As particles hit the steel layers, they generate a shower of new particles. The plastic scintillators then produce photons, which are converted into an electric current proportional to the original particle's energy. The Tile Calorimeter includes approximately 420,000 plastic scintillator tiles read out by 9500 photomultiplier tubes and weighs close to 2900 tonnes, making it the heaviest component of the ATLAS experiment. The central barrel is constructed from 64 wedges, each 5.6m long, and two extended barrels each

with 64 wedges, each 2.6m long. Geometrically it occupies a transverse radius from 2.28-4.25m from the interaction point. A summary of the calorimeter properties can be found in table 3.1.

Calorimeter	Material	Pseudorapidity	Thickness
LAr EM barrel	lead-LAr	$|\eta| < 1.5$	24 X_0
LAr EM end-cap	lead-LAr	$1.4 < |\eta| < 3.2$	26 X_0
LAr hadronic end-cap	copper-LAr	$1.5 < |\eta| < 3.2$	12 λ
LAr forward	copper/tungsten-LAr	$3.1 < |\eta| < 4.9$	9 λ
Tile barrel	iron-scintillator	$|\eta| < 1.0$	11 λ
Tile extended barrel	iron-scintillator	$0.8 < |\eta| < 1.7$	11 λ

Table 3.1: The ATLAS Calorimeter's subsection's properties. Common to each subsection is a composition of: a metal to induce showers and an excitable layer to collect energy from the showers. [73][46]

3.2.5   Muon Spectrometer

Situated around the calorimeters, the Muon Spectrometer (MS) measures the momentum of muons by detecting their deflected tracks, caused by the magnetic field of the large superconducting air-core toroid magnet system described in section 3.2.2.

The MS houses four types of gaseous radiation detectors, arranged according to the structure of the toroid magnet and is segmented into 16 parts in azimuth. These detectors can be categorized into two groups: precision and trigger chambers. Precision chambers, comprising Monitored Drift Tube (MDT) and Cathode Strip Chamber (CSC) detectors, allow for precise measurement of the muon tracks as they pass through the MS. This precise measurement in the bending plane of these tracks enables accurate determination of the muon momenta via their curvature.

The trigger chambers, made up of Resistive Plate Chamber (RPC) and Thin Gap Chamber (TGC) detectors, facilitate fast signal formation and readout times. This rapid readout assists in accurately associating a passing muon with a specific proton-
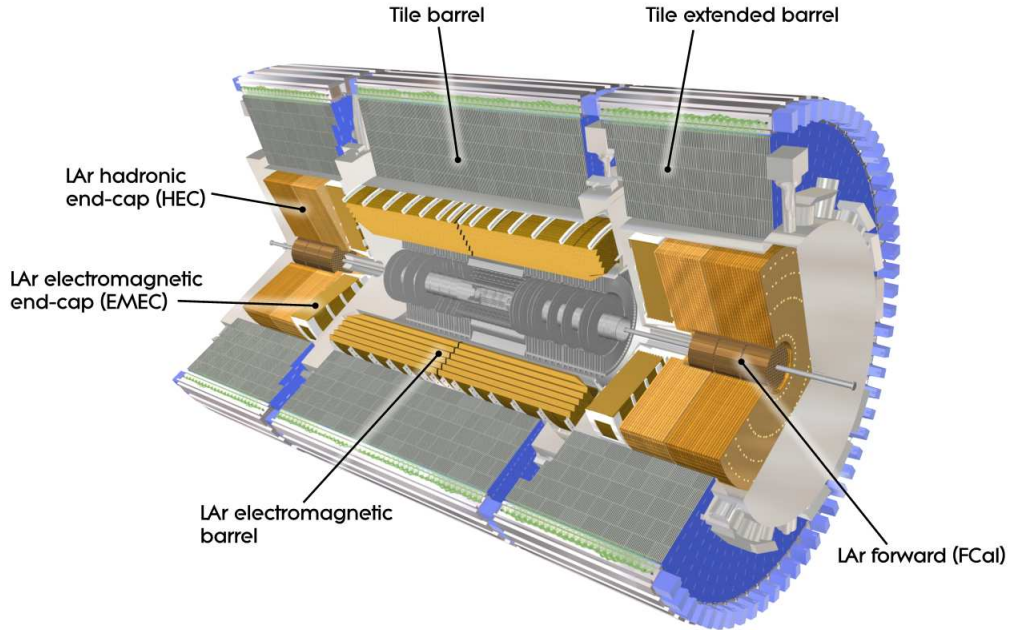
Figure 3.9: A diagram of the ATLAS calorimeters. The liquid argon barrel, end-cap and forward calorimeters form the inner layer (gold) and are surrounded by the hadronic tile calorimeter (grey). [74]

proton bunch crossing. Both types of detectors exist in the barrel and end-cap sections of the MS, with at least three layers of precision-type chambers spread over the entire $|\eta|$ range of the MS. The general layout of the MS is shown in figure 3.10.

The precision chambers in the barrel section of the MS are rectangular, arranged in three concentric cylindrical shells around and parallel to the beam axis at radial distances of 5, 7.5, and 10.5 meters [75]. These precision chambers consist of MDT chambers with tubes perpendicular to the beam axis and parallel to the toroidal magnetic field, providing precise measurements along η.

The end-cap muon chambers, located in $1 < |\eta| < 2.7$, extend radially in four rings or "wheels", arranged concentrically with the beam axis at different distances from the interaction point. Like in the barrel section, the primary precision measurement in the end-caps is given by MDT chambers which are located in all four wheels of the end-cap. However, in the region $2 < |\eta| < 2.7$, which experiences the highest background rates, precision muon measurement is provided by CSC chambers [76].

These chambers can resolve spatial information in both η and ϕ, and due to their high granularity readout structure, can sustain higher background rates in this forward region of the detector. A summary of the regions covered by the different components of the muon spectrometer can be found in table 3.2.

The MDT chambers use a gas mixture of 93% Argon and 7% CO2, with a single tungsten-rhenium wire operated at 3 kV. When a minimum ionizing particle (MIP) passes through the tube, it ionizes the gas, the charge from which is read out as the signal. The MDT chambers are designed as multi-layers of these tubes, helping to improve the spatial resolution down to 50 µm.

The CSC detectors in the end-cap are multi-wire proportional chambers, operating with a gas mixture of Argon, CO2, and CF4. They are structured with cathode strips perpendicular to anode wires, providing spatial information in both η and ϕ directions. CSC chambers can achieve a spatial hit resolution of approximately 60 µm due to their multi-layered structure.

In both barrel and end-cap sections, the trigger chambers play a vital role in forming muon trigger decisions. The RPC chambers serve this purpose in the barrel, while the end cap's trigger chambers consist of the TGC detectors. RPC chambers work with a gap of 2mm filled with tetrafluorethane (C2H2F4), lined with parallel plate electrodes operated at a potential difference of 9.8 kV. This setup allows a timing resolution of 2 ns. TGC detectors, on the other hand, function as multi-wire proportional chambers with a gas mixture of CO2 and n-pentane (n-C5H12). Operated at a potential difference of 2.9 kV, TGC detectors are able to read out signals with a timing resolution of 4 ns [48].

3.2.6 Trigger System

The LHC produces collisions at a high frequency of 40 MHz during its operational cycle. Due to the complex nature of the detector systems, including all subsystems of ATLAS, a single collision event generates approximately 1.5 MB of data. Conse-
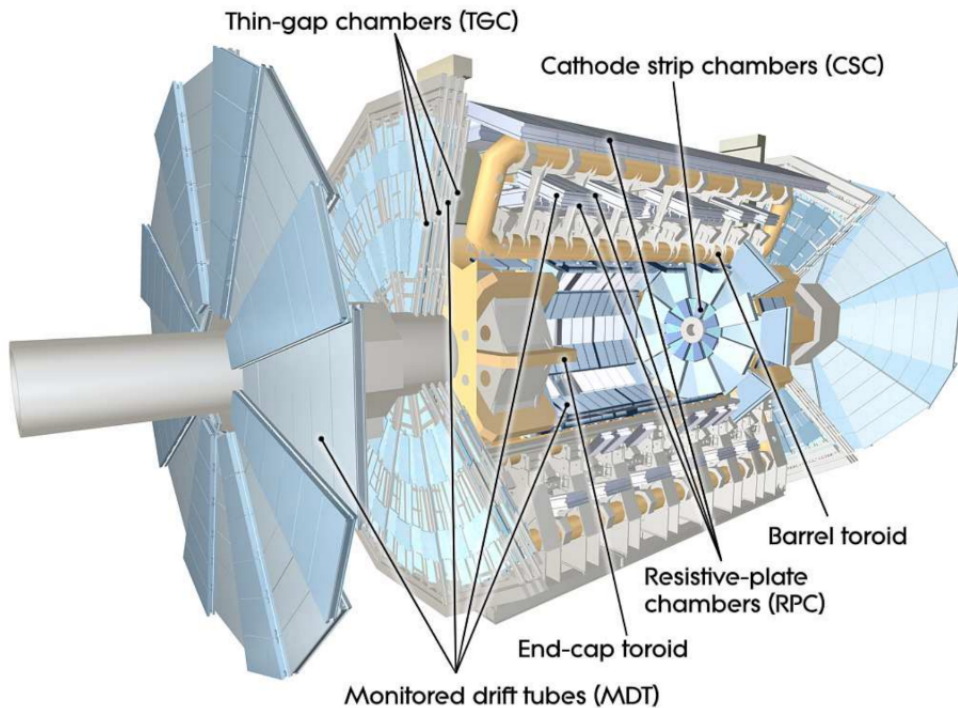
Figure 3.10: A cutaway diagram of the ATLAS detector that labels the various subsections of the muon spectrometer [1][77].

Detector	Function	Coverage	Chambers	Channels
MDT	Precision tracking	$|\eta| < 2.0$	1150	354000
CSC	Precision tracking	$2.0 < |\eta| < 2.7$	32	31000
RPC	Triggering	$|\eta| < 1.05$	606	373000
TGC	Triggering	$1.05 < |\eta| < 2.4$	3588	318000

Table 3.2: Summary of the ATLAS muon spectrometer subsections.

quently, considering the collision frequency, ATLAS would have to handle data rates in the range of 60 TB per second if every event were to be recorded.

Such an overwhelming amount of data is not just technically challenging to manage and store, but also unnecessary for scientific research, as the majority of the collision events are classified as soft parton scattering occurrences. These events typically do not contain significant physics phenomena worthy of detailed study.

To combat these challenges, the ATLAS experiment utilizes a system known as the trigger to selectively identify and store potentially interesting events. This system aims to reduce the data rate to a more manageable level that can be processed for further analysis.

The ATLAS trigger system comprises two distinct levels: the Level 1 (L1) trigger and the High-Level Trigger (HLT). The L1 trigger is a hardware-based system that rapidly screens collision data using coarse measurements collected from the calorimeters and the muon spectrometer. It is designed to make a preliminary event filtering decision within 2.5 μs of the bunch crossing.

The main task of the L1 trigger is to identify events that involve high transverse momentum (p_T) leptons, photons, jets, and significant total or missing transverse energy, while also filtering for events that originate at the interaction point. It achieves this by defining Regions of Interest (RoI) in the detector where unusual or intriguing features have been detected. The L1 trigger's decision-making process is performed by the central trigger processor (CTP), which also has the capability to perform prescaling, reducing the rate of events passing a nominal L1 decision by a constant factor. Overall, the L1 trigger aims to decrease the event rate from the LHC's crossing frequency of 40 MHz to a target rate of 100 kHz.

Events that are successfully selected by the L1 trigger are then passed to the High-Level Trigger (HLT). The HLT is a software-based system that performs more detailed filtering of the data by reconstructing physics objects in a rudimentary manner. To achieve this, it utilizes all of the available detector data within the RoI's identified by

the L1 system, operating at full granularity and precision.

The HLT significantly reduces the rate of events written out to approximately 1 kHz, which corresponds to roughly one out of every 40,000 collision events being saved. These selected events are subsequently transferred to the Tier-0 computing facility at CERN for offline reconstruction and analysis [78].

Chapter 4

The Proposed ADAM Detector and Its Simulation

In order to make predictions within the framework of the SM or alternative theoretical frameworks we must make detailed models of the events being studied and the detector output expected when these events occur. To do this we must first generate events according to the model in question using a monte carlo event generator. Pythia [79] is a general-purpose event generator capable of simulating hard scattering events as well as soft parton showering events. For this simulation, I use Pythia 8.3 [79][80] to generate hard scattering events, which describe the collision of partons to generate the process of interest, an outgoing stau / anti-stau pair $(pp \rightarrow \tilde{\tau}\bar{\tilde{\tau}})$, ignoring hadronization as it is not relevant given the nature of the scenario considered where the stau decays long after the generating event.

Pythia requires a spectrum of masses of the supersymmetric particles under a given set of model parameters. As explained in section 2.3.4 the masses of SUSY particles can be obtained by numerically solving the renormalization group equations. This is done using SoftSUSY 4.1 [81][82] and then provided to Pythia in the form of a SUSY Les Houches Accord 2 (SLHA2) file [83].

The next stage in the simulation chain involves modelling the passage of the particle through the matter that makes up the ATLAS detector. This modelling is accomplished with the Geant4 toolkit [15], which simulates the passage of particles through

matter and is the standard for detector simulation in high-energy physics. Geant4 is a general-purpose detector simulator and requires the user to define the detector geometry, materials, and/or applied fields.

The ATLAS collaboration maintains detailed databases of the detector geometry [84] in the form of SQL-lite databases. In this simulation, the database with tag geometry-ATLAS-R3S-2021-03-02-00 was used. Geant4 however, does not include a means to read this database file. To construct a Geant4 simulation using the database the tool FullSimLight [16] was used. FullSimLight is a submodule of the GeoModel [85] suite of tools, a standalone, detector-agnostic version of tools used by the ATLAS collaboration in their official software Athena [86]. FullSimLight also facilitates the implementation of the ATLAS magnetic field map and any functionalities contained in Geant4 via "plug-ins" that can be defined by the user.

Figure 4.1 shows the level of detail of the simulation, which contains 117,922 objects, ranging from steel and aluminum support structures down to layers of Kapton tape.

In this simulation, the FTFP_BERT [87][88] Geant4 physics list was used along with modifications to define the supersymmetric stau and gravitino particles. In the implementation of the stau particle, it is assumed that it will interact with matter similarly to how a SM heavy charged particle (eg. tau) would, depositing its energy in the detector via scattering [89] and ionization [90].

4.1 The ADAM Detector

The proposed Auxiliary Detector above the ATLAS Muon spectrometer (ADAM) is the detector studied in this simulation. Its purpose is to detect the decays of very long-lived stau particles ($\tau = $ 7-365 days) that have been produced in 14 TeV proton-proton collisions and subsequently become trapped in the ATLAS detector material. This detector would be monitored during times when the LHC beam is off, such as annual shutdowns or intermittent technical stops during normal operations. By doing
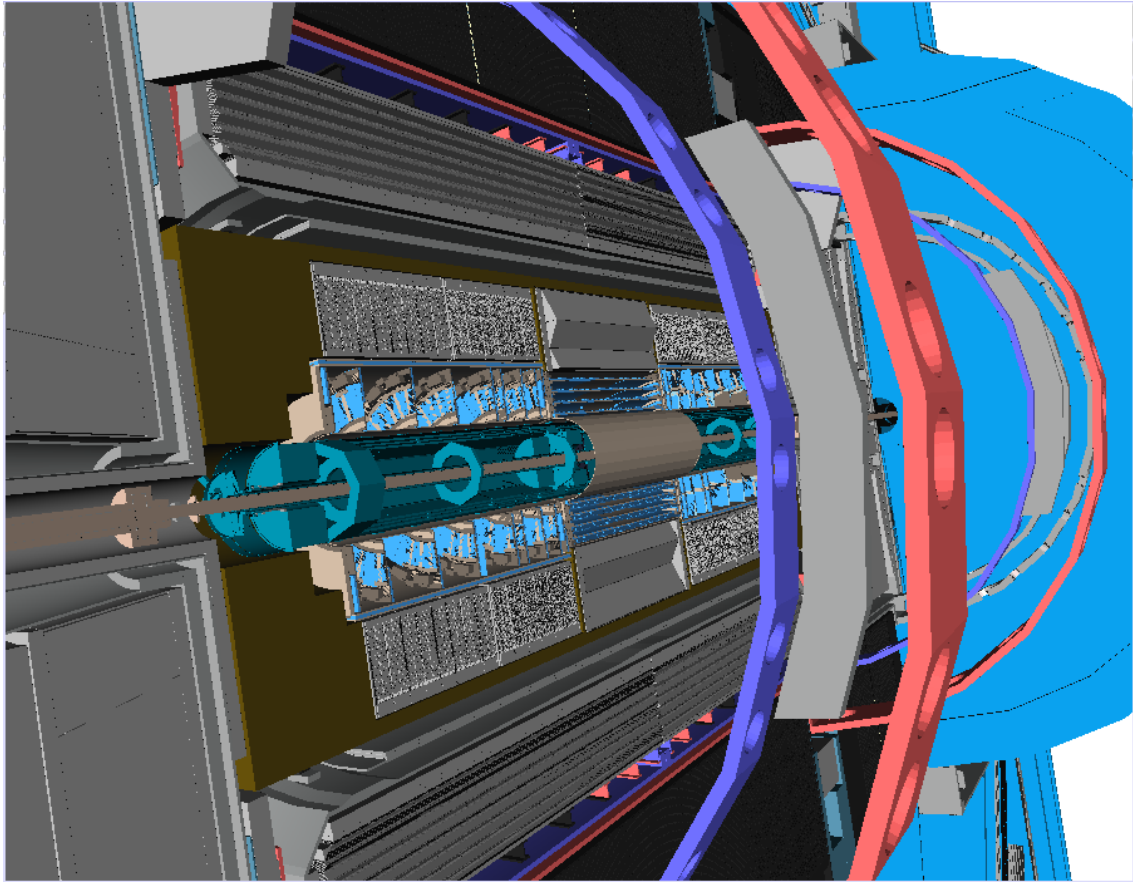
Figure 4.1: A close-up, cutaway view of the model of the ATLAS inner detector and calorimeters in GeoModel Explorer showing the level of detail.

this the primary source of backgrounds due to SM particles from the IP is eliminated. Since the lifetimes considered in this simulation are so long, provided enough events are produced, decay signals would be present during beam-off periods.

The ADAM detector is pictured in figure 4.2 and would consist of two regions of three, 12.5 mm thick planes of plastic scintillator spaced 30 cm apart with wavelength shifting fibres embedded in an x-y pattern, which would be read out by silicon photomultipliers (SiPM). The pitch of the fibres in either direction will be 1 cm, Figure 4.3 shows a close-up rendering of the three-layer structure and fibre layout. As particles pass through the plastic scintillator and cause scintillation light, this light can then enter the fibres where secondary scintillation occurs isotropically, ensuring some light undergoes total internal reflection in the fibre and is delivered to the SiPM. By taking the strongest signals produced in any x-y fibre pair we can assume the incident particle travelled closest to this fibre pair giving a 1 cm resolution. This provides the minimum resolution case as much finer granularity may be possible by interpolating a position based on the relative intensity in the highest intensity pair's nearest neighbours or beyond.

The first region of the ADAM detector sits closest to the ATLAS detector at a radius between 13.0-13.6 m (measured from the panel center) consisting of 3 subregions, each 7.2 m in width, one normal with the y-axis and 2 at $-36°$. The second region, which would be mounted on the ATLAS cavern ceiling and would occupy a radius from 22.9-23.5 m, with 9 subregions, each with a width ranging from 3.8-3.9 m, the center region being normal to the y-axis and each successive flanking panel at $-11.25°$ to the last. The length of all the panel subregions in the z direction is 45.0 m for a total area of 7612 m^2, which implies 39584 wavelength shifting fibres with a total linear length of 38.3 km, or double this number for dual fibres in each channel. Although not studied here, of note is that, by using two separate regions, this creates a decay volume of approximately 12,980 m^3 to explore other scenarios such as neutral particles decaying in flight.

Particles passing through the panels at close to the speed of light will take more than 1 ns to traverse the 30 cm panel spacing, a timing resolution that is achievable with SiPMs, allowing for a directional track to be created from hits on the panel. By doing this, we can differentiate between upwards-going tracks originating in ATLAS from downward-going tracks caused by cosmic rays. Given the ability to isolate cosmic muon signals, this may also provide a second use case for ADAM as a device to study cosmic muon showers, or to trigger the ATLAS detector to study comic muon events which do not point at the interaction point. However, the focus of this study is to evaluate ADAM as a detector for very long-lived charged particles and in this scenario identifying cosmic muon events serves the purpose of effectively eliminating background, leaving only very rare upward-going muons induced by neutrinos passing through the earth [91].

To construct the simulation of ADAM a Geometry Description Markup Language (GDML) [92] file is created to contain the measurements of the individual panels in the detector as well as their placement in space, and the materials they are comprised of. This file is then converted to an SQL-Lite database and concatenated with the official ATLAS geometry using tools in the GeoModel toolkit. The detector geometry is reviewed in figure 4.2.

Customized plugins for the tracking of particles in the Geant4 simulation and the instantiation of ADAM as a "sensitive detector" within Geant4 were written and used within FullSimLight.

4.2   Event Timing

In this simulation, the LHC run 4 and long shutdown 4 are the target window for the study. Given the possible lifetimes of up to one year, the distribution of events in time is a crucial aspect of this study. The premise of making measurements according to the LHC's beam-off times given by the LHC schedule in figure 3.4 requires generating events sequentially in time, however, Geant4, by default, generates events with a
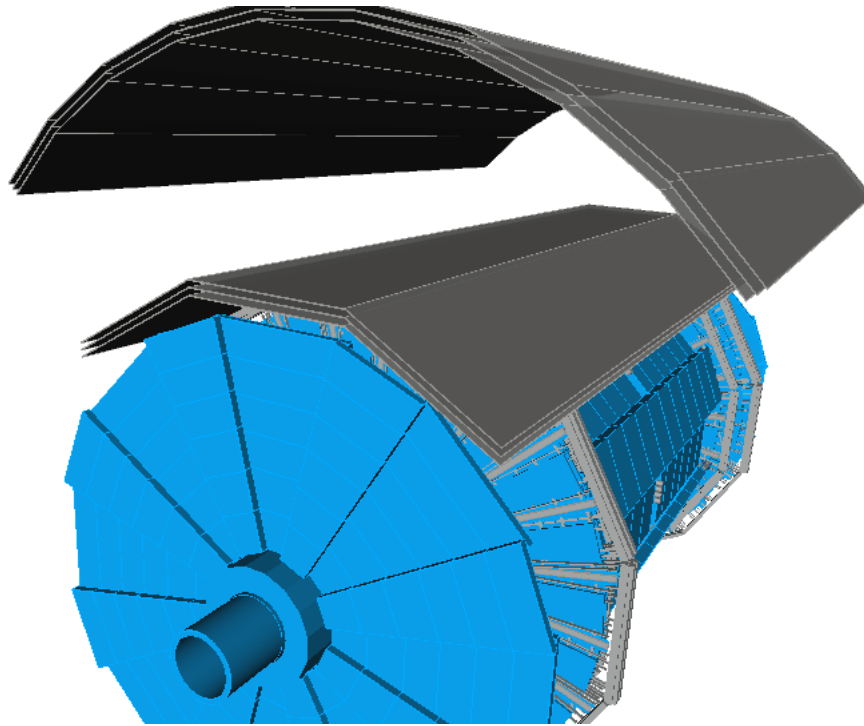
Figure 4.2: A 3D model of the ATLAS detector (blue) and the ADAM detector (dark grey) placed above.

Figure 4.3: A 3D CAD model of a module containing 3 horizontal plastic scintillating panels, wavelength shifting fibres and a support structure. These modules would be combined to form the panel subregions shown in Figure 4.2.

global time of $t = 0$ for each event, and then allows particles like the stau to decay at a later time which is sampled from an exponential lifetime distribution.

To correct the times, distributing them along the LHC schedule, we first use Pythia to determine the cross-section for the $pp \to \tilde{\tau}\bar{\tilde{\tau}}$ process at a given $M_{1/2}$ parameter. This cross-section is then used in equation 3.3 with the projected run 4 integrated luminosity of 715 fb^{-1} to determine the total number of events. A "map" of the LHC schedule is created where the proton physics, ion physics, beam commissioning and shutdown times are divided, and the events are then randomly distributed in the proton physics portions. More specifically, the output data of the Geant4 simulation, which includes the creation time and decay time of trapped staus, and thus of the daughter tau and gravitino, are shifted by this time. For example, if Geant4 produces a stau which decays after 7 days, that event is then assigned a random time during the proton physics windows, for ease assume this is 1 month into the first block of time, then this particle will have a creation time of 1 month and a decay time of 1 month and 7 days.

4.2.1   Magnetic Field

The simulation is run using the ATLAS magnetic field map. This is important since the stau is a charged particle and the strong magnetic fields in the solenoid and toroid magnets will influence its trajectory.

These magnets are active systems that require cryogenic cooling and as such are not in operation during long shutdowns. To model this change in the magnetic field over the course of the operational schedule we first record the stopping position of trapped staus in the ATLAS detector, the time they decay at, and the direction of momentum of the resulting tau lepton. Due to technical limitations, Geant4 cannot change the magnetic field in the simulation according to an irregular pattern. Therefore, we allow the simulation to run to completion with the magnetic on, and then run a second simulation with the magnetic field map off, starting from the production of

the tau lepton using the same momentum generated in the first run.

4.3   Event Acceptance Criteria

In the Geant4 simulation, the ADAM detector is defined as a "sensitive detector" allowing for an action to be taken when a particle is present in the volume the detector occupies. In our case this results in a printout of a particle's coordinates, its energy, and the amount of energy it has deposited in the detector. If the particle does not deposit any energy in the detector, which is the case with neutrinos and can be the case with some photons, they are not recorded. Figures 4.4 and 4.5 show two example events.

Because staus may come to rest in the outer edges of ATLAS, and then decay isotropically, it is possible that the decay products, either because of angle or range, may travel through one region of the ADAM detector but not both. If the recorded data satisfies the condition that a coordinate is generated in either all three bottom layers, or all three top layers, and these are not separated in time by more than 100ns, this is accepted as an event. As mentioned in section 4.1, the ADAM detector is multi-purpose and can be used to study other types of events such as the decay of neutral non-interacting particles in flight, this is achieved via the large decay volume it establishes, however, for the study of decays coming from below, i.e. within the ATLAS detector, the decay volume is not necessary, the tri-layer construction of each of the two regions of ADAM make either capable of independently reconstructing a pointing track based on the timing of hits on the three panels, hence why we only require that decay products interact with all three panels of one region.
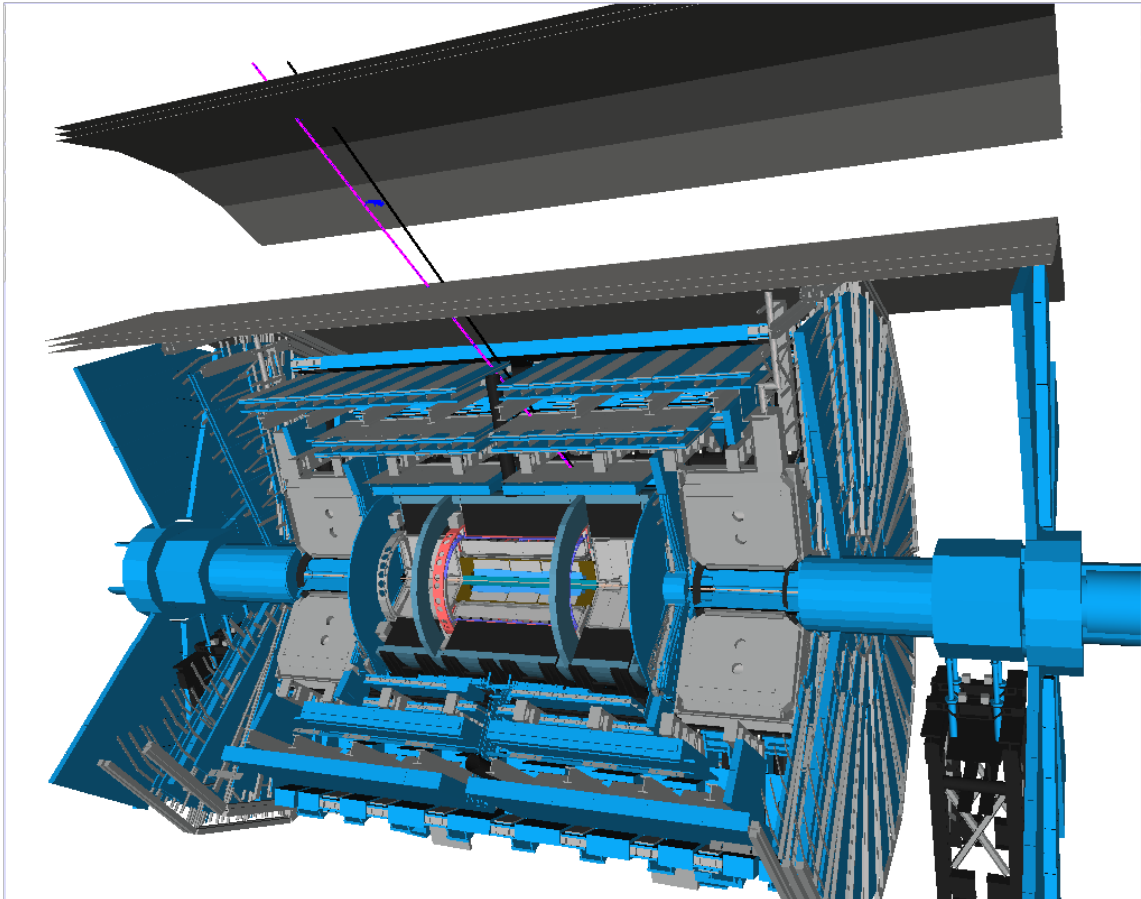
Figure 4.4: The track of a detected event is shown in the GeoModel Explorer. Part of the geometry is cut away to show the origin of the particle tracks somewhere in the tile calorimeter. In this instance the decay products are minimal, the stopped stau will have decayed to a SM tau particle which decays rapidly into its second most common branching (10.82%), a charged pion (magenta) and tau neutrino (black).
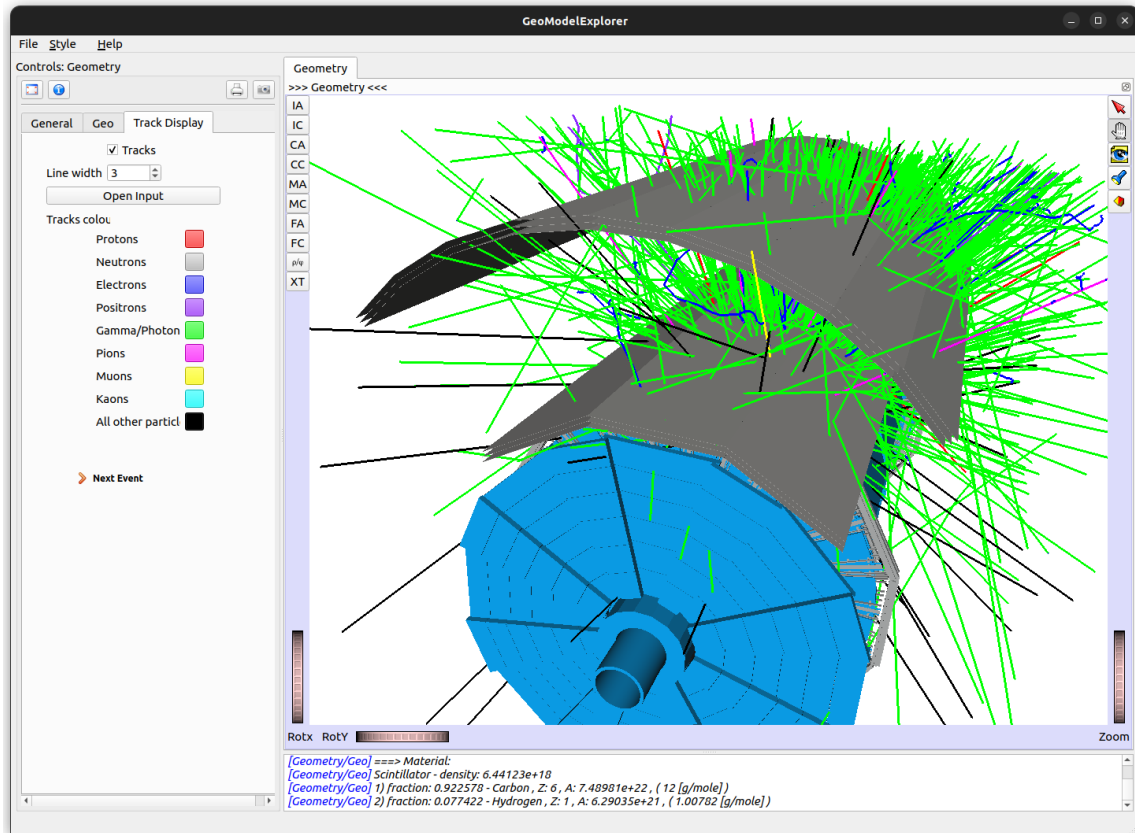
Figure 4.5: Some events are much more densely populated due to electromagnetic showers caused by the decays. In this event, we see a large flux of photons (green). A color legend of the different particle types is displayed in GeoModel Explorer displayed on the left.

Chapter 5

Analysis

5.1 Model Parameters

As mentioned in sections 2.3.5 and 2.3.6, the parameter space of the mSUGRA model in which the stau is the NLSP includes the range of parameters where $m_0 = A_0 = 0$, $\tan\beta = 10$, $\text{sgn}\,(\mu) > 0$, and the value of $M_{1/2}$ is in a range from $300 - 1300$ GeV. Using these parameters, and incrementing the value of $M_{1/2}$ by 100 GeV, the calculator SoftSusy returns a stau mass between 112-477 GeV. Within each of these mass spectra, the gravitino mass is calculated by solving equation 2.2 for $m_{\tilde{G}}$ with lifetimes of 7, 30, 90, 150, and 365 days which results in a Gravitino mass of 4-27 GeV at the lowest $M_{1/2}$ value and 135-327 GeV at the highest, a graph of the relationship between the $M_{1/2}$ parameter, the lifetime, and the resulting particle masses is shown in figure 5.1.

The increased mass of the stau in the higher $M_{1/2}$ range is correlated with a lower cross-section and number of events as shown in figure 5.2.

5.2 Stau Trapping

After generating events via Pythia, FullSimLight passes these events to Geant4 where the detector geometry is built and the stau particle's passage through the detector material is simulated. In the Geant4 simulation, when particles have ~ 0 MeV of energy their tracking is "killed" and data such as the particle's coordinates, and the
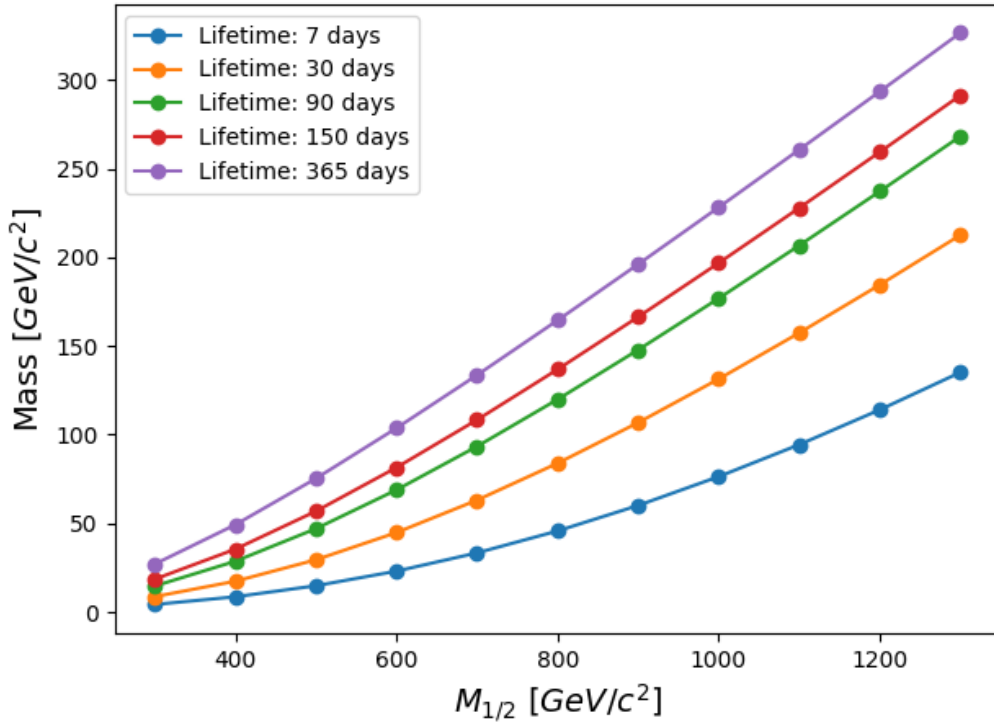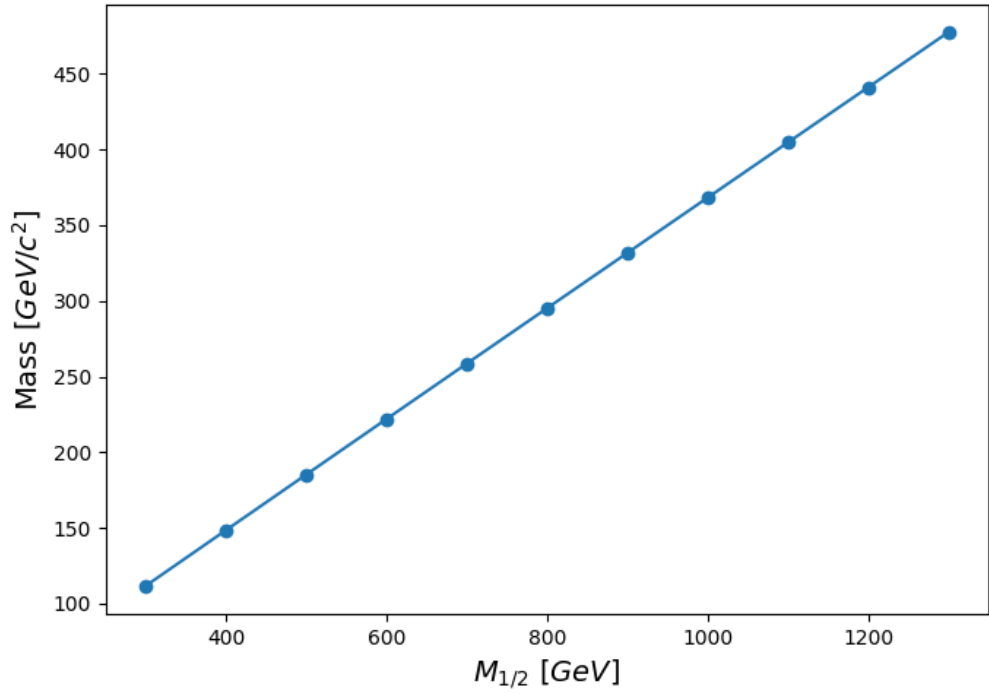
Figure 5.1: Top: The resulting stau masses for given values of M$_{1/2}$ in the mSUGRA model. Bottom: Each line shown represents a lifetime of the stau particle, which sets the gravitino mass in the model. At M$_{1/2}$ = 1300 GeV and the lifetime 1 year, the combined mass of the stau and gravitino is over 800 GeV.
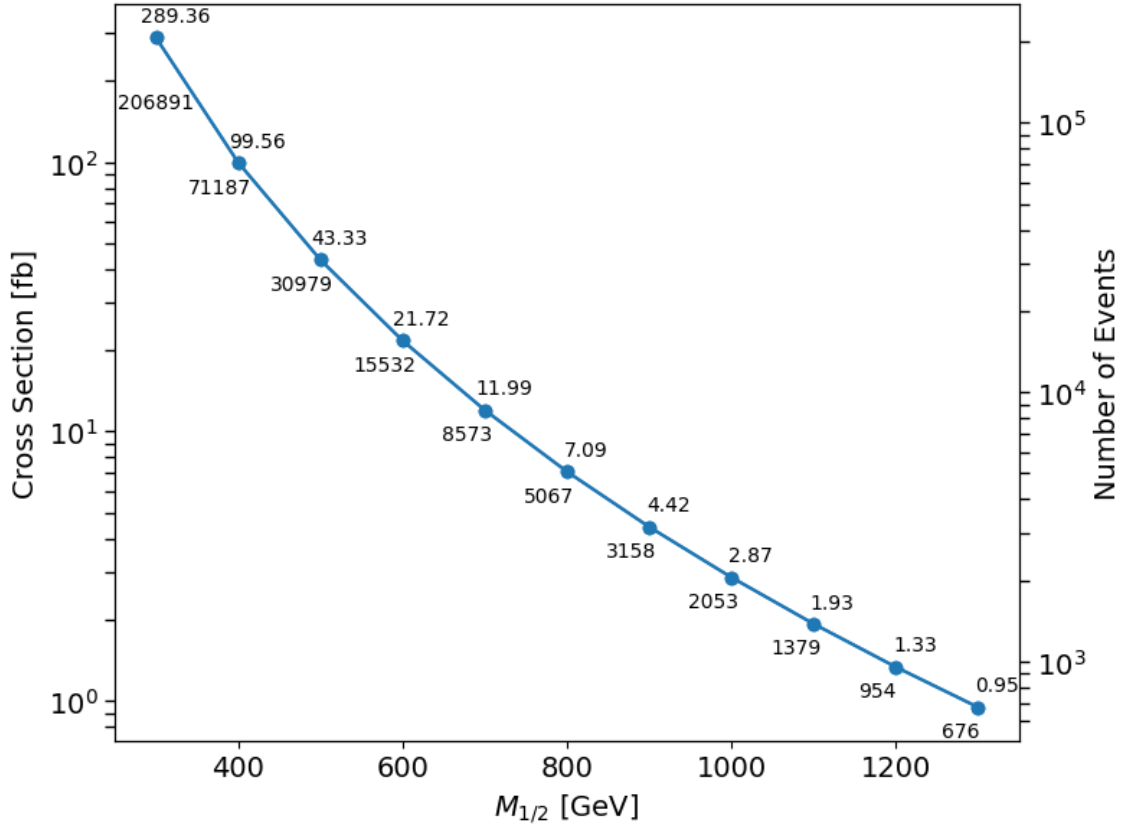
Figure 5.2: A semi-log plot of the maximum cross section for the $pp \to \tilde{\tau}\bar{\tilde{\tau}}$ process as given by Pythia, and the number of events given the anticipated 715 fb^{-1} of integrated luminosity over run 4. The upper numbers give the cross section in femtobarns and the bottom numbers are the number of events based on 715 fb^{-1} of integrated luminosity.

geometric volume it is contained can be recorded. In our simulation, if the material of the containing volume is not air, the particle is considered trapped and is entered into the dataset.

In figure 5.3 we can see the angular distribution of the produced staus. Most staus that are produced follow a path in the direction of the beam pipe and do not stop in the detector, however, those that have proportionally more of their momenta in the transverse direction also have a low energy which often results in them being trapped. Figure 5.4 shows the distribution of energies for the produced staus. We can see from figure 5.3 that most of the stopped staus have a momentum direction between $\pi/4$ - $\pi/2$, which corresponds to between the diagonal and completely transverse. As well, once in this region, the distribution of momenta is mostly flat.

The proportion of stopped staus is dependent on the model used. In figure 5.5 we can see that at the lower mass values the particles are more likely to be stopped, even when normalized according to the number of staus produced. We know from figure 5.2 that the production rate falls off exponentially with the $M_{1/2}$ parameter, however, the fraction of stopped staus also follows an (albeit less steep) exponential decay, that quickly levels off. An additional table of the fraction of staus which stop, per $M_{1/2}$ value is shown in table A.1. At a $M_{1/2}$ of 500 GeV there is an anomalous drop in the number of trapped staus, which remains true even when 10^6 events are run.

The ATLAS calorimeters are described in section 3.2.4, where their material composition and purpose of stopping particles are explained. With this in mind, it is easy to predict that most staus will stop within the calorimeters, which is the case.

In particular, the vast majority of staus stop in the iron/steel of the hadronic tile calorimeter. Table 5.1 shows that $\sim 75\%$ stop here. As well, in figures 5.6 and 5.7 this is illustrated.
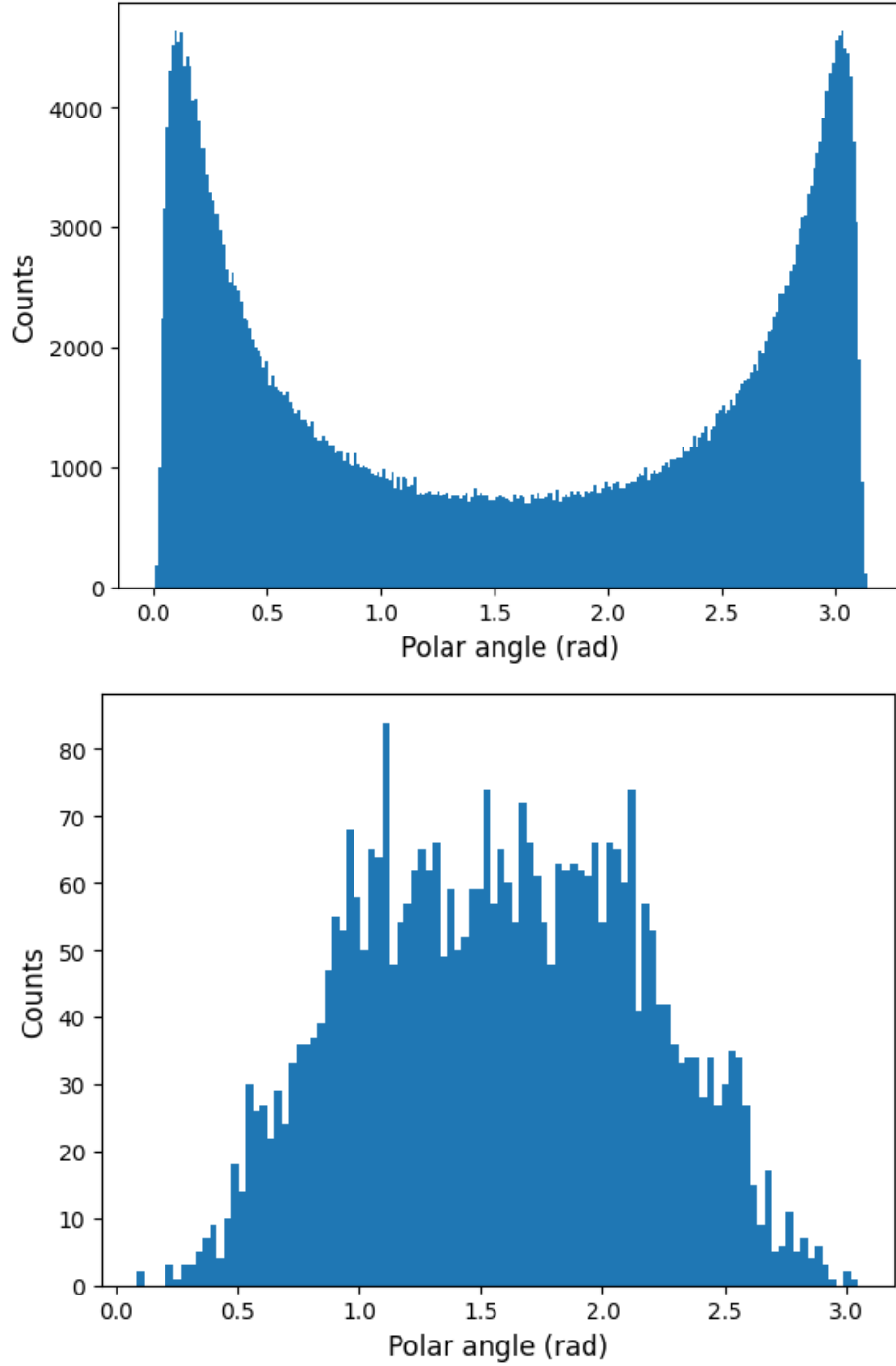
Figure 5.3: Top: The angular distribution of all produced stau momenta. Bottom: The angular distribution of *starting* momenta for those staus which have stopped in the detector. These graphs show the example case when $M_{1/2} = 300$ GeV and the lifetime is 30 days. For higher values of $M_{1/2}$ fewer staus are produced, but qualitatively the distribution remains. As explained in section 3.2.1, the polar angle is in the z direction at 0 and π, eg down the beam pipe. We see from this graph that most events travel down the beam pipe.

53
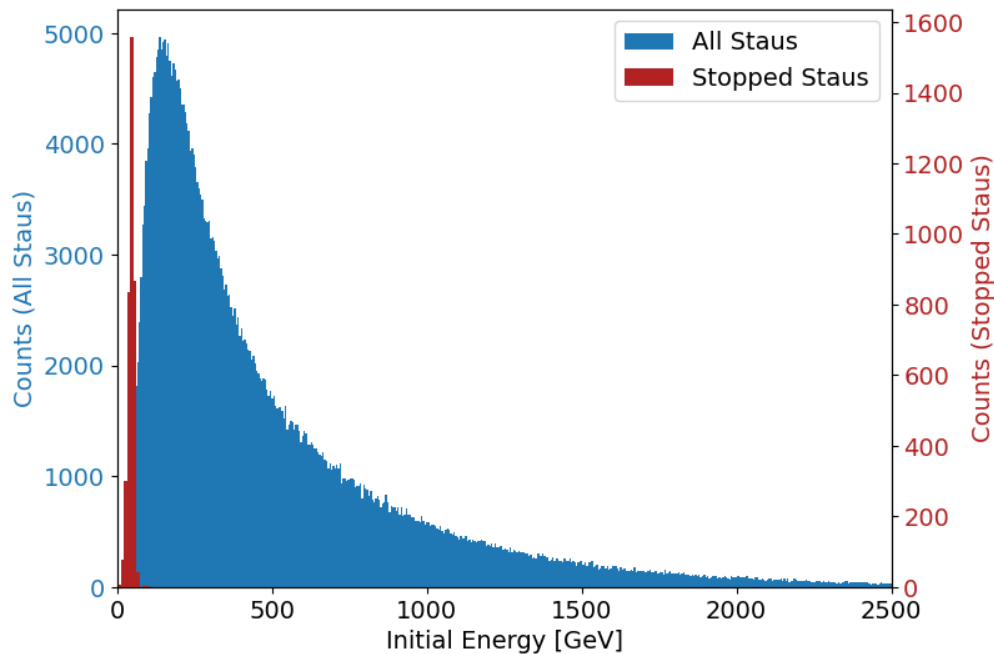
Figure 5.4: The initial energy of produced staus. The left axis corresponds to the initial energy of all staus produced, and the right axis, scaled for illustration, corresponds to the initial energy of those staus which later stopped in the detector.

Material	Staus Stopped (%)
Iron/Steel	74.9 ± 0.4
Aluminium	10.3 ± 0.4
Scintillator	3.7 ± 0.2
Liquid Argon	3.6 ± 0.2
Lead	1.95 ± 0.09

Table 5.1: The five most common materials staus come to rest in. The values are averaged over all values of $M_{1/2}$.
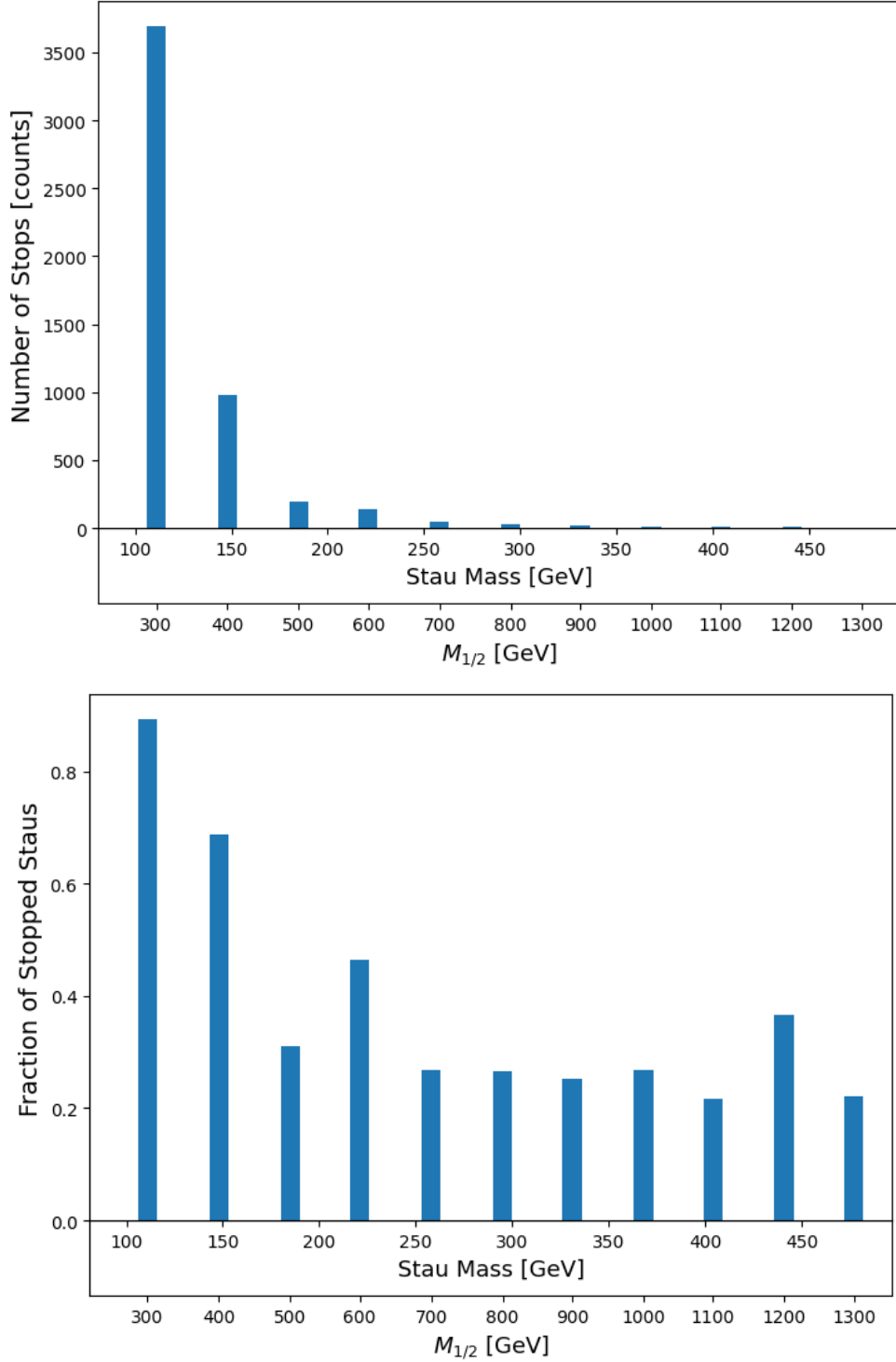
Figure 5.5: The population of staus that come to rest in the detector for each of the evaluated model parameters. Top: The total number of stau stopped. We know from figure 5.2 that the production rate falls off exponentially and therefore the stopped population does as well. A table of values can be found in appendix A. Bottom: The fraction of produced staus that stop also appears to follow an exponential decrease, independent of the cross-section.
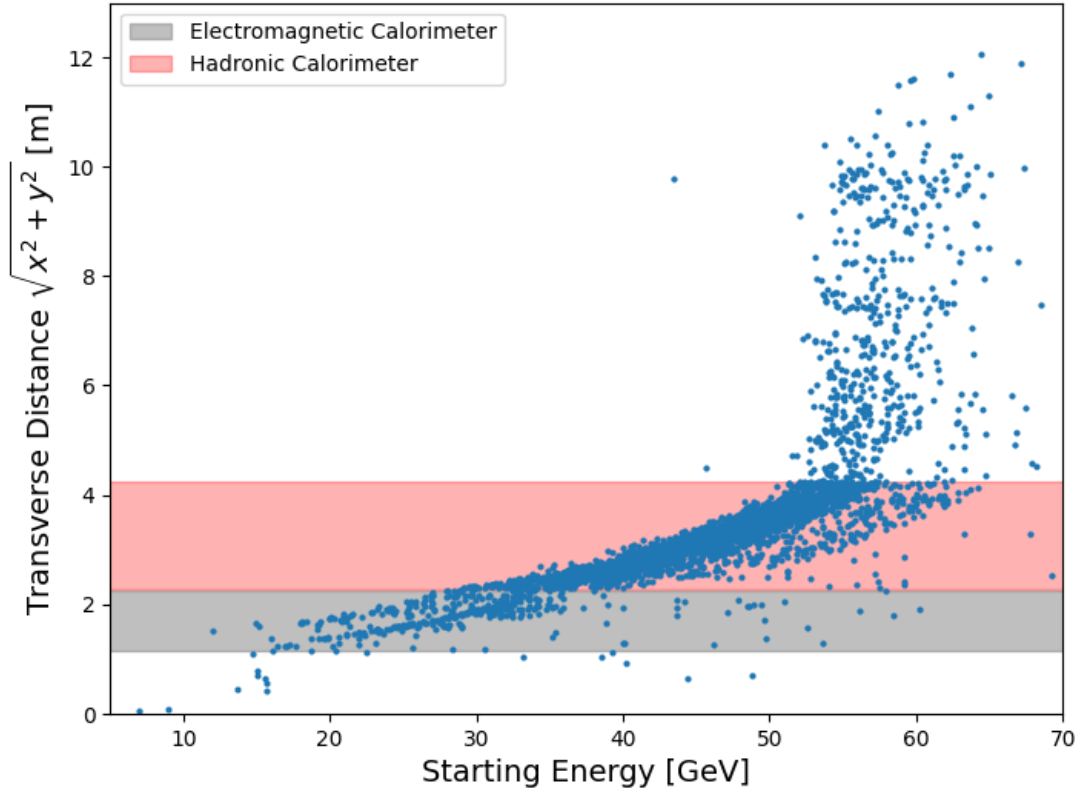
Figure 5.6: Using the parameter $M_{1/2} = 300\,\text{GeV}$ with lifetime 30 days as an example, the penetrating depth of the staus based on their initial energy is shown. The plot has been cropped to show with clarity where the majority of staus stop. At very high energy there are just a handful of outliers that also stop in the calorimeters. For the energy range that mostly comes to rest in the muon spectrometer, a small number of staus actually come to rest in the ADAM detector itself.
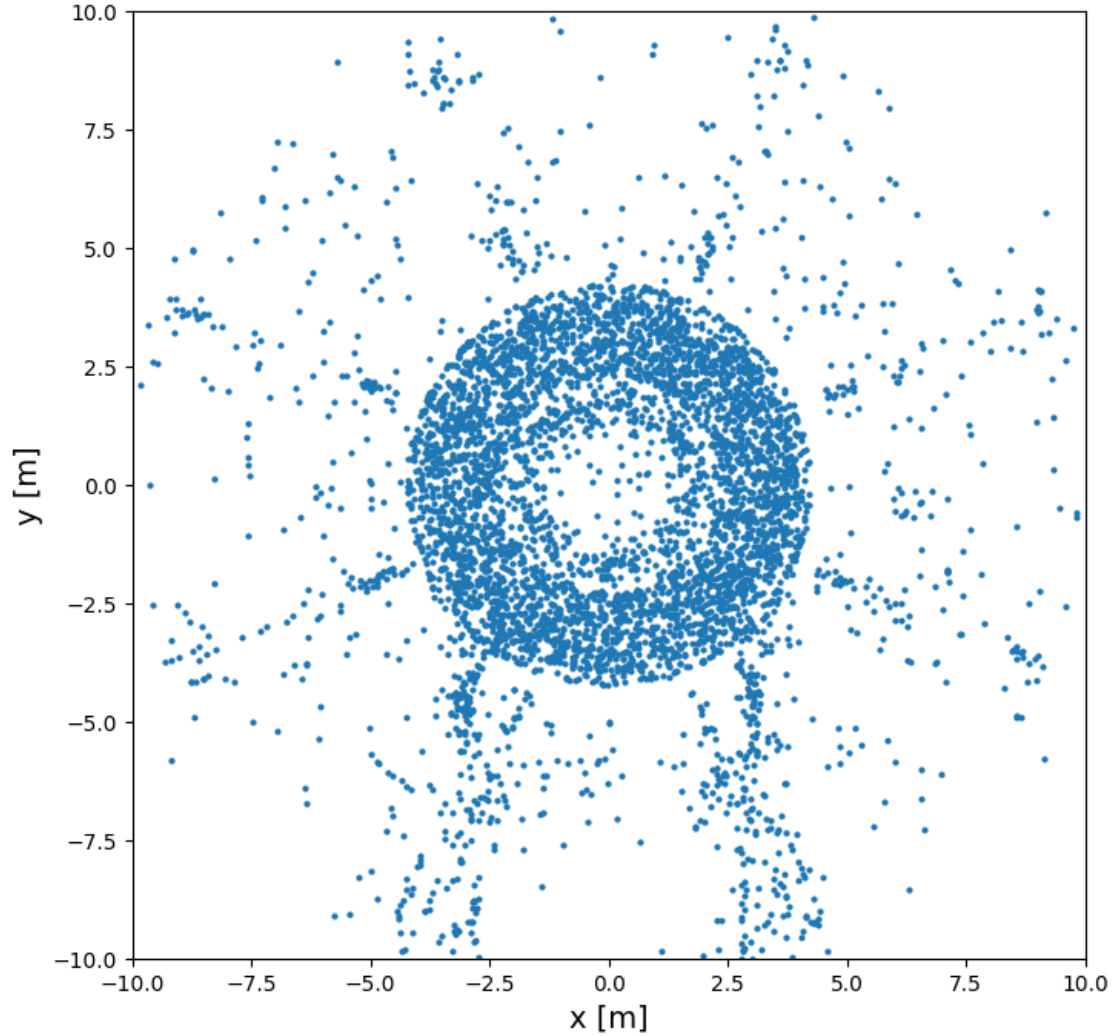
Figure 5.7: A symmetric plot of the stopping positions in the x-y plane. For illustrative purposes, this plot is created using the $M_{1/2} = 500$ GeV parameter with 10^6 events. The positions trace out the hadronic calorimeter where most staus stop, with a small gap between it and the electromagnetic calorimeter, which also captures a significant number of the staus. The support structures underneath ATLAS can also be seen as these are primarily made of aluminum and iron/steel. Finally, faint outlines of the axial regions of the barrel toroid in the muon spectrometer region are visible.
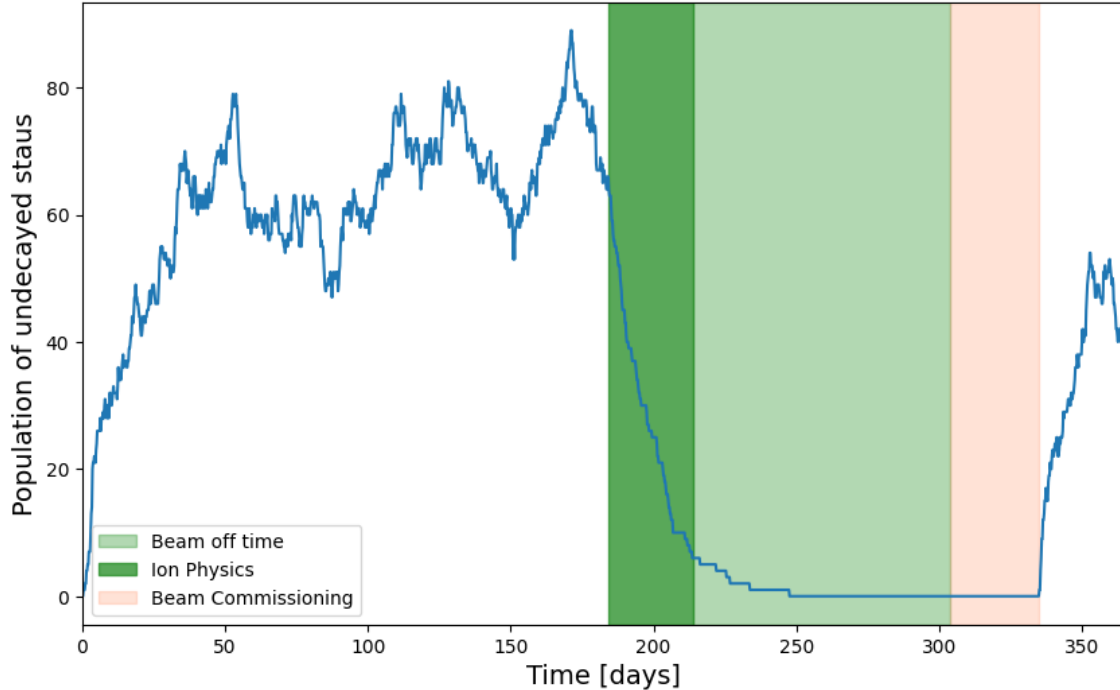
Figure 5.8: A graph of the population of trapped, undecayed staus in the detector over time in this example with the parameters $M_{1/2} = 300$ GeV and a lifetime of 30 days. The technical stop or "beam off time" is highlighted in light green.

5.3 Decay Detection

As mentioned in section 4.1 the ADAM detector will monitor for the decays of trapped particles during year end shutdowns and intermittent technical stops. Working under this assumption, and with the timing schedule of event generation and decay described in 4.2 we can filter out stau decays that occur during times where there will be background present, e.g. during proton-proton collisions, ion collisions and beam commissioning.

Nomillay, each period of proton-proton physics is followed by one month of ion physics, as shown in figure 3.4. During these times various configurations are used, such as lead-lead collisions at energies of 2.75 TeV/nucleon [93]. Given the energy level, we assume that no staus are generated during these times, however, these events do produce significant radiation which would be a background for the decays we wish to measure. Therefore, we exclude these times from the times we expect to be able

to monitor the ADAM detector for decay signals. When the stau lifetime is short, this severely limits the number of observable events, since most staus decay during the month of ion physics. This is illustrated in figure 5.8 which shows the population of trapped stau particles in the ATLAS detector over the course of a year.

In the first year of run 4, based on our model with the parameters $M_{1/2} = 300$ GeV and a lifetime of 30 days we expect 107,102 staus to be produced and there to be 915 trapped, of these 32 will decay during the first long technical stop between Dec 2029 - Feb 2030. We will discuss the number of these we expect to detect below but first, we would point out that when the lifetime is 7 days, this drops to 0 decays during the shutdown.

5.3.1   Detecting During Normal Operations

As mentioned in section 3.1.1 the LHC beam is not a continuous stream of particles but consists of a train of particle bunches. With each revolution about the LHC ring, a portion collide at the interaction points. Over time, the population of bunches decreases and the beam needs to be refilled. The refill times offer an opportunity to make measurements of stau decays outside of the regular long technical stops.

Publicly available beam intensity data in figure 5.9 shows the pattern of beam fill-decay cycles. Each cycle has an activity period that is, by rough approximation, 2/3 of one day and is followed by a short period of inactivity, about one hour in length, though the activity periods are often shorter and followed by much longer inactivity periods. Therefore, a conservative estimate of the inactive periods is three one-hour periods, every two days.

During these times, the solenoid and toroid magnetic fields will still be on as the process of cryogenically cooling the magnets happens on a scale of days, and therefore it is not practical to switch off for short periods of time (see: figure B.1). This has implications for our simulation, however, as explained in section 4.2.1. As a consequence of the program structure of Geant4, we are required to simulate each
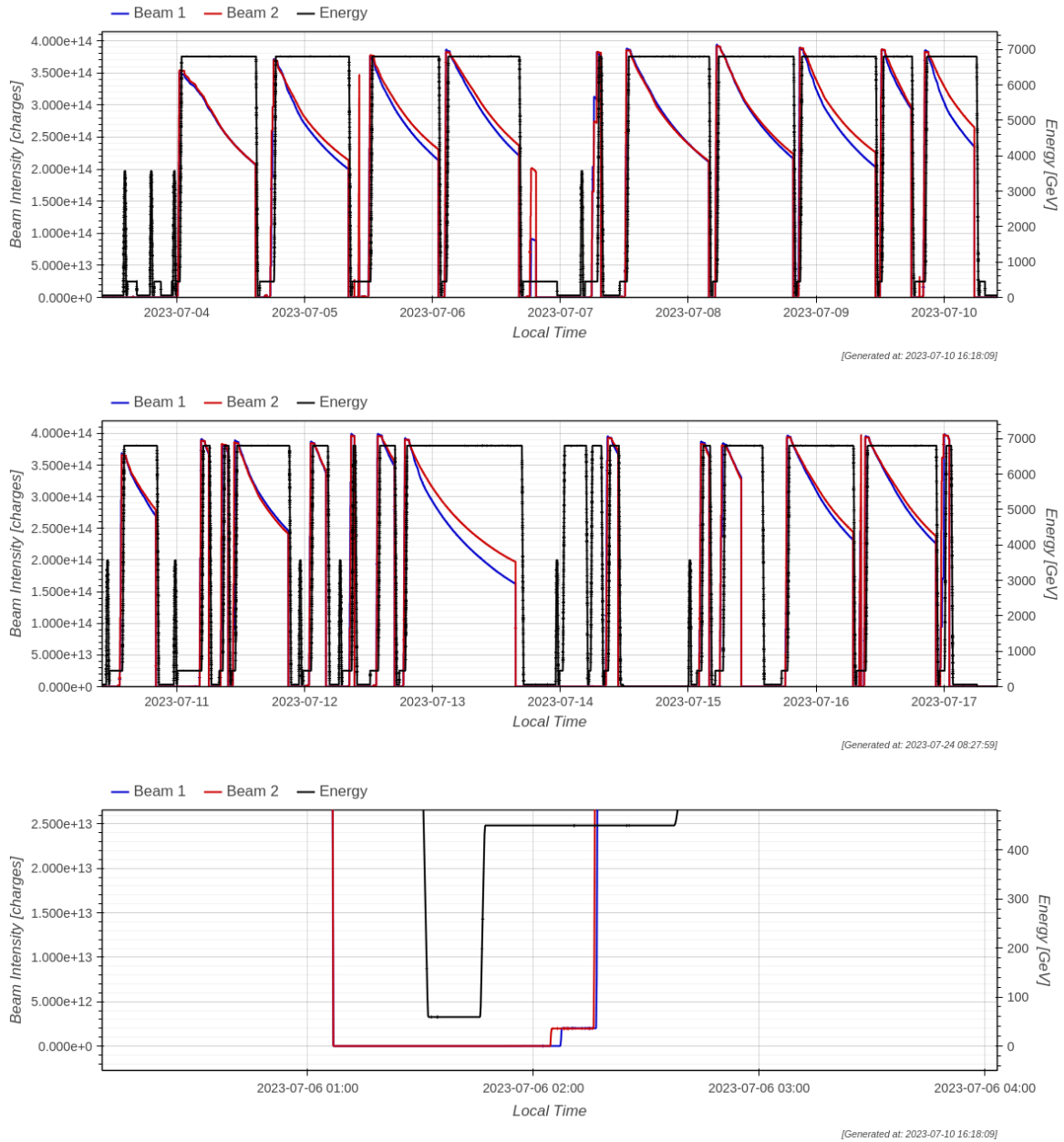
Figure 5.9: Top/Middle: LHC Beam intensity data from the weeks of July 02-15 2023 (Run 3). These plots show that the beam is off periodically. Bottom: a close-up of the width of the smallest window of beam off time, which is approximately one hour.

stau decay's daughter particles twice: once with the ATLAS magnetic field on and once with it off.

With this in mind, we expand our window of acceptance conservatively to include randomly distributed windows of one hour occurring on average three times per two days. Events during these times are tagged as events with the magnetic field on. When including these periods, the number of stau decays occurring during background-free periods increases markedly; in the case of $M_{1/2} = 300$ GeV with a 7-day lifetime, the increase is from zero to 99.7 ± 0.4 events over the course of run 4, on average. A table of the separated year-end vs intermittent stop decays can be found in table C.1.

5.4 Acceptance of the ADAM Detector for Stau Physics at the LHC

After accounting for the cross-sections predicted by the model and the expected run 4 integrated luminosity, along with a random production rate during the run 4 proton physics windows, and based on the operational schedule for the LHC with the adjustments described in section 5.3.1 we are able to report in table 5.2 the expected number of recorded events with the ADAM detector during background free monitoring, under the different parameter scenarios considered.

This analysis involves choosing both random times for the staus to be produced within the proton physics windows of the LHC schedule and choosing random short intervals for monitoring, in addition to the periods during year-end shutdowns. This choice of random times was repeated 1000 times for each of the 55 model parameter points studied and the results averaged.

From table 5.2 we can see the range of expected events recorded by the ADAM detector. The value of 0 at some of the parameter space reflects the fact that at high values of $M_{1/2}$ the number of events produced is very low (as shown in figure 5.2), and less than 1% of those produced stop in the ATLAS detector. Those which are produced may then decay during the proton-proton, ion physics, or beam commis-

M_{12} $\diagdown$ τ	7	30	90	150	365
300	11.7 ± 0.5	14.8 ± 0.5	52.6 ± 0.7	75.7 ± 0.8	132.3 ± 0.9
400	3.9 ± 0.4	5.6 ± 0.5	12.8 ± 0.5	25.7 ± 0.5	42.0 ± 0.6
500	0.7 ± 0.4	0.7 ± 0.4	2.6 ± 0.4	7.9 ± 0.5	10.0 ± 0.5
600	0.7 ± 0.4	0.7 ± 0.4	3.7 ± 0.5	3.7 ± 0.4	7.2 ± 0.5
700	0.2 ± 0.4	0.2 ± 0.4	0.3 ± 0.3	1.4 ± 0.4	2.4 ± 0.4
800	0.1 ± 0.5	0.2 ± 0.4	0.2 ± 0.3	0.3 ± 0.3	0.3 ± 0.3
900	0.1 ± 0.5	0.1 ± 0.4	0.4 ± 0.4	0.8 ± 0.5	1.1 ± 0.4
1000	0.0 ± 0.3	0.0 ± 0.4	0.6 ± 0.6	0.3 ± 0.4	1.1 ± 0.5
1100	0.0 ± 0.4	0.0 ± 0.3	0.1 ± 0.3	0.4 ± 0.4	1.6 ± 0.6
1200	0.0 ± 0.4	0.0 ± 0.4	0.0 ± 0.2	0.4 ± 0.5	0.4 ± 0.4
1300	0	0	0	0	0

Table 5.2: The expected total events recorded with the ADAM detector over the course of run 4, during background free times.

sioning periods which are not background-free. Even with these restrictions, we see that at longer lifetime values and lower values of $M_{1/2}$ the ADAM detector is sensitive in this area of the parameter space, with greater than 3 events detected for all of the $M_{1/2}$=300, 400 GeV space and much of 500 and 600 GeV, which correspond to stau masses of 112, 148, 185, and 222 GeV respectively.

Chapter 6

Conclusion

In this work, we have performed a simulation of the production of supersymmetric particles, staus, under a minimal supergravity scenario, at the High Luminosity LHC during run 4. Using the full ATLAS geometry and magnetic field we have simulated the passage of these particles through the detector and estimated that for stau masses between 112-477 GeV that 0.89 - 0.22% of the produced particles will become trapped in the detector.

We have proposed the construction of an Auxiliary Detector above the ATLAS Muon spectrometer (ADAM) to detect the subsequent decays of these stau particles which may have a lifetime between 7-365 days. Our study is conducted under a specific scenario which includes the production of stau particles as predicted by a minimal supergravity model at the High Luminosity LHC. Here we account for the predicted cross-section of the $pp \rightarrow \tilde{\tau}\bar{\tilde{\tau}}$ process, the expected run 4 integrated luminosity, and the operating schedule of the LHC. We find that for some areas of the parameter space studied, we may expect up to record 132.3 ± 0.9 events with the detector, and that for all lifetimes studied with stau masses less than 148 GeV we would achieve at least 3 detections. This may extrapolate to other BSM theories which predict a heavy ($\mathcal{O}(100)$ GeV), charged, scalar particle. Additionally, our cosmological constraints on the lifetime of the stau, restricting it to less than 1 year, may be alleviated in other scenarios. Our results indicate a higher sensitivity to longer lifetimes, therefore

a more model-independent search in the future with greater lifetimes may produce even stronger results.

In this thesis, we have also alluded to other possible applications of the ADAM detector. As mentioned in 4.1 it creates a 13,000 m^3 decay volume for the detection of neutral particles decaying in flight, which is a suggested scenario of study for future works. The results from our analysis show a strong possibility for the detection of charged scalar particles below 100 GeV. Other models that also feature an exceptionally long lifetime and have masses below this threshold would be of interest for further study as well.

Bibliography

[1]   G Aad *et al.*, "The atlas experiment at the cern large hadron collider," *Journal of Instrumentation*, vol. 3, no. 08, S08003, 2008. DOI: 10.1088/1748-0221/3/08/S08003. [Online]. Available: https://dx.doi.org/10.1088/1748-0221/3/08/S08003.

[2]   S Chatrchyan *et al.*, "The CMS experiment at the CERN LHC. The Compact Muon Solenoid experiment," *JINST*, vol. 3, S08004, 2008, Also published by CERN Geneva in 2010. DOI: 10.1088/1748-0221/3/08/S08004. [Online]. Available: https://cds.cern.ch/record/1129810.

[3]   G. Aad *et al.*, "Observation of a new particle in the search for the standard model higgs boson with the ATLAS detector at the LHC," *Physics Letters B*, vol. 716, no. 1, pp. 1–29, 2012. DOI: 10.1016/j.physletb.2012.08.020. [Online]. Available: https://doi.org/10.1016%2Fj.physletb.2012.08.020.

[4]   S. Chatrchyan *et al.*, "Observation of a new boson at a mass of 125 GeV with the CMS experiment at the LHC," *Physics Letters B*, vol. 716, no. 1, pp. 30–61, 2012. DOI: 10.1016/j.physletb.2012.08.021. [Online]. Available: https://doi.org/10.1016%2Fj.physletb.2012.08.021.

[5]   R. N. Cahn, "The eighteen arbitrary parameters of the standard model in your everyday life," *Rev. Mod. Phys.*, vol. 68, pp. 951–959, 3 1996. DOI: 10.1103/RevModPhys.68.951. [Online]. Available: https://link.aps.org/doi/10.1103/RevModPhys.68.951.

[6]   S. M. Bilenky, "Neutrino in standard model and beyond," *Physics of Particles and Nuclei*, vol. 46, no. 4, pp. 475–496, 2015. DOI: 10.1134/S1063779615040024. [Online]. Available: https://doi.org/10.1134/S1063779615040024.

[7]   B. A. Robson, "The matter-antimatter asymmetry problem," *Journal of High Energy Physics, Gravitation and Cosmology*, vol. 04, no. 01, 166–178, 2018, ISSN: 2380-4327. DOI: 10.4236/jhepgc.2018.41015.

[8]   A. Arbey and F. Mahmoudi, "Dark matter and the early universe: A review," *Progress in Particle and Nuclear Physics*, vol. 119, p. 103 865, 2021, ISSN: 0146-6410. DOI: https://doi.org/10.1016/j.ppnp.2021.103865. [Online]. Available: https://www.sciencedirect.com/science/article/pii/S0146641021000193.

[9] J. L. Feng, "Naturalness and the status of supersymmetry," *Annual Review of Nuclear and Particle Science*, vol. 63, no. 1, pp. 351–382, 2013. DOI: 10.1146/annurev-nucl-102010-130447. [Online]. Available: https://doi.org/10.1146%2Fannurev-nucl-102010-130447.

[10] G. L. Kane, "Supersymmetry: What? why? when?" *Contemporary Physics*, vol. 41, no. 6, pp. 359–367, 2000. DOI: 10.1080/00107510010001644. eprint: https://doi.org/10.1080/00107510010001644. [Online]. Available: https://doi.org/10.1080/00107510010001644.

[11] S. P. Martin, "A Supersymmetry primer," *Adv. Ser. Direct. High Energy Phys.*, vol. 18, G. L. Kane, Ed., pp. 1–98, 1998. DOI: 10.1142/9789812839657_0001. arXiv: hep-ph/9709356.

[12] J. L. Feng, S. Su, and F. Takayama, "Supergravity with a gravitino lightest supersymmetric particle," *Phys. Rev. D*, vol. 70, p. 075019, 7 2004. DOI: 10.1103/PhysRevD.70.075019. [Online]. Available: https://link.aps.org/doi/10.1103/PhysRevD.70.075019.

[13] J. L. Feng, "Dark matter candidates from particle physics and methods of detection," *Annual Review of Astronomy and Astrophysics*, vol. 48, no. 1, pp. 495–545, 2010. DOI: 10.1146/annurev-astro-082708-101659. eprint: https://doi.org/10.1146/annurev-astro-082708-101659. [Online]. Available: https://doi.org/10.1146/annurev-astro-082708-101659.

[14] J. L. Feng, S. Iwamoto, Y. Shadmi, and S. Tarem, "Long-lived sleptons at the LHC and a 100 TeV proton collider," *Journal of High Energy Physics*, vol. 2015, no. 12, pp. 1–24, 2015. DOI: 10.1007/jhep12(2015)166. [Online]. Available: https://doi.org/10.1007%2Fjhep12%282015%29166.

[15] S. Agostinelli *et al.*, "GEANT4–a simulation toolkit," *Nucl. Instrum. Meth. A*, vol. 506, pp. 250–303, 2003. DOI: 10.1016/S0168-9002(03)01368-8.

[16] Bandieramonte, Marilena, Bianchi, Riccardo Maria, and Boudreau, Joseph, "Fullsimlight: Atlas standalone geant4 simulation," *EPJ Web Conf.*, vol. 245, p. 02029, 2020. DOI: 10.1051/epjconf/202024502029. [Online]. Available: https://doi.org/10.1051/epjconf/202024502029.

[17] I. J. R. Aitchison and A. J. G. Hey, *Gauge Theories in Particle Physics: A Practical Introduction, Volume 1 : From Relativistic Quantum Mechanics to QED, Fourth Edition*. Taylor & Francis, 2013, ISBN: 978-1-4665-1302-0, 978-0-429-18538-0, 978-1-4665-1299-3. DOI: 10.1201/b13717.

[18] S. E. et al., "Review of particle physics," *Physics Letters B*, vol. 592, no. 1, pp. 1–5, 2004, Review of Particle Physics, ISSN: 0370-2693. DOI: https://doi.org/10.1016/j.physletb.2004.06.001. [Online]. Available: https://www.sciencedirect.com/science/article/pii/S0370269304007579.

[19] G. F. Giudice, "Naturally speaking: The naturalness criterion and physics at the lhc," in *Perspectives on LHC Physics*, pp. 155–178. DOI: 10.1142/9789812779762_0010. eprint: https://www.worldscientific.com/doi/pdf/10.1142/9789812779762_0010. [Online]. Available: https://www.worldscientific.com/doi/abs/10.1142/9789812779762_0010.

[20] U. User:MissMJ, *Standard model of elementary particles*, [Online - Wikipedia; accessed July 14, 2023], September, 2019. [Online]. Available: https://en.wikipedia.org/wiki/File:Standard_Model_of_Elementary_Particles.svg.

[21] L. Boyle, *Standard model of particle physics–most complete diagram*, [Online - Wikipedia; accessed July 14, 2023], 2014. [Online]. Available: https://commons.wikimedia.org/wiki/File:Standard_Model_Of_Particle_Physics--Most_Complete_Diagram.png.

[22] D. J. Griffiths, *Introduction to elementary particles; 2nd rev. version* (Physics textbook). New York, NY: Wiley, 2008. [Online]. Available: https://cds.cern.ch/record/111880.

[23] G. Gabrielse, "The standard model's greatest triumph," *Physics Today*, vol. 66, no. 12, pp. 64–65, Dec. 2013, ISSN: 0031-9228. DOI: 10.1063/PT.3.2223. eprint: https://pubs.aip.org/physicstoday/article-pdf/66/12/64/15826275/64_1_online.pdf. [Online]. Available: https://doi.org/10.1063/PT.3.2223.

[24] E. Hubble, "A relation between distance and radial velocity among extra-galactic nebulae," *Proceedings of the national academy of sciences*, vol. 15, no. 3, pp. 168–173, 1929.

[25] A. G. Riess *et al.*, "Observational evidence from supernovae for an accelerating universe and a cosmological constant," *The Astronomical Journal*, vol. 116, no. 3, p. 1009, 1998. DOI: 10.1086/300499. [Online]. Available: https://dx.doi.org/10.1086/300499.

[26] M. Li, X.-D. Li, S. Wang, and Y. Wang, *Dark energy: A brief review*, 2012. arXiv: 1209.0922 [astro-ph.CO].

[27] Q. R. Ahmad *et al.*, "Direct evidence for neutrino flavor transformation from neutral-current interactions in the sudbury neutrino observatory," *Phys. Rev. Lett.*, vol. 89, p. 011301, 1 2002. DOI: 10.1103/PhysRevLett.89.011301. [Online]. Available: https://link.aps.org/doi/10.1103/PhysRevLett.89.011301.

[28] Y. Fukuda *et al.*, "Evidence for oscillation of atmospheric neutrinos," *Physical review letters*, vol. 81, no. 8, p. 1562, 1998.

[29] M. E. Peskin, *Supersymmetry in elementary particle physics*, 2008. arXiv: 0801.1928 [hep-ph].

[30] I. J. R. Aitchison, *Supersymmetry in Particle Physics. An Elementary Introduction.* Cambridge: Cambridge University Press, 2007, ISBN: 978-0-511-61925-0. DOI: 10.1017/CBO9780511619250.

[31] C. CSÁ KI, "THE MINIMAL SUPERSYMMETRIC STANDARD MODEL," *Modern Physics Letters A*, vol. 11, no. 08, pp. 599–613, 1996. DOI: 10.1142/ s021773239600062x. [Online]. Available: https://doi.org/10.1142%2Fs021773239600062x.

[32] M. e. a. "Aaboud, "Search for supersymmetry in events with four or more leptons in $\sqrt{s}$ = 13 TeV *pp* collisions with ATLAS," *Phys. Rev. D*, vol. 98, p. 032 009, 2018, 47 pages in total, author list starting page 31, 9 figures, 8 tables, published in Phys. Rev. D, all figures including auxiliary figures are available at https://atlas.web.cern.ch/Atlas/GROUPS/PHYSICS/PAPERS/SUSY-2016-21/. DOI: 10.1103/PhysRevD.98.032009. arXiv: 1804.03602. [Online]. Available: https://cds.cern.ch/record/2312374.

[33] H. Baer and D. B. Cline, "Dark matter from SUGRA GUTs: mSUGRA, NUSUGRA and yukawa-unified SUGRA," in *AIP Conference Proceedings*, AIP, 2009. DOI: 10.1063/1.3232200. [Online]. Available: https://doi.org/10.1063%2F1.3232200.

[34] M. Fairbairn, A. Kraan, D. Milstead, T. Sjöstrand, P. Skands, and T. Sloan, "Stable massive particles at colliders," *Physics Reports*, vol. 438, no. 1, pp. 1– 63, 2007. DOI: 10.1016/j.physrep.2006.10.002. [Online]. Available: https://doi.org/10.1016%2Fj.physrep.2006.10.002.

[35] J. L. Feng, A. Rajaraman, and F. Takayama, "Probing gravitational interactions of elementary particles," *Int. J. Mod. Phys. D*, vol. 13, pp. 2355–2359, 2004. DOI: 10.1142/S0218271804006474. arXiv: hep-th/0405248.

[36] J. L. Feng and B. T. Smith, "Slepton trapping at the cern large hadron collider and the international linear collider," *Physical Review D*, vol. 71, no. 1, 2005, ISSN: 1550-7998. DOI: 10.1103/physrevd.71.015004.

[37] T. Moroi, H. Murayama, and M. Yamaguchi, "Cosmological constraints on the light stable gravitino," *Physics Letters B*, vol. 303, no. 3, pp. 289–294, 1993, ISSN: 0370-2693. DOI: https://doi.org/10.1016/0370-2693(93)91434-O. [Online]. Available: https://www.sciencedirect.com/science/article/pii/037026939391434O.

[38] L. Evans and P. Bryant, "Lhc machine," *Journal of Instrumentation*, vol. 3, no. 08, S08001, Aug. 2008. DOI: 10.1088/1748-0221/3/08/S08001. [Online]. Available: https://dx.doi.org/10.1088/1748-0221/3/08/S08001.

[39] *ATLAS magnet system: Technical Design Report, 1* (Technical design report. ATLAS). Geneva: CERN, 1997. DOI: 10.17181/CERN.9O5C.VDTM. [Online]. Available: https://cds.cern.ch/record/338080.

[40] *ATLAS end-cap toroids: Technical Design Report* (Technical design report. ATLAS). Geneva: CERN, 1997, Electronic version not available. DOI: 10.17181/ CERN.P03D.WQLV. [Online]. Available: https://cds.cern.ch/record/331066.

[41] J. P. Badiou, J Beltramelli, J. M. Baze, and J Belorgey, *ATLAS barrel toroid: Technical Design Report* (Technical design report. ATLAS). Geneva: CERN, 1997, Electronic version not available. DOI: 10.17181/CERN.RF2A.CP5T. [Online]. Available: https://cds.cern.ch/record/331065.

[42] *ATLAS central solenoid: Technical Design Report* (Technical design report. AT-LAS). Geneva: CERN, 1997, Electronic version not available. DOI: 10.17181/ CERN.ZZVJ.2JYE. [Online]. Available: https://cds.cern.ch/record/331067.

[43] N. Wermes and G Hallewel, *ATLAS pixel detector: Technical Design Report* (Technical design report. ATLAS). Geneva: CERN, 1998. [Online]. Available: https://cds.cern.ch/record/381263.

[44] *ATLAS inner detector: Technical Design Report, 1* (Technical design report. ATLAS). Geneva: CERN, 1997. [Online]. Available: https://cds.cern.ch/record/ 331063.

[45] S Haywood, L Rossi, R Nickerson, and A Romaniouk, *ATLAS inner detector: Technical Design Report, 2* (Technical design report. ATLAS). Geneva: CERN, 1997. [Online]. Available: https://cds.cern.ch/record/331064.

[46] *ATLAS liquid-argon calorimeter: Technical Design Report* (Technical design report. ATLAS). Geneva: CERN, 1996. DOI: 10.17181/CERN.FWRW.FOOQ. [Online]. Available: https://cds.cern.ch/record/331061.

[47] *ATLAS tile calorimeter: Technical Design Report* (Technical design report. AT-LAS). Geneva: CERN, 1996. DOI: 10.17181/CERN.JRBJ.7O28. [Online]. Available: https://cds.cern.ch/record/331062.

[48] *ATLAS muon spectrometer: Technical Design Report* (Technical design report. ATLAS). Geneva: CERN, 1997. [Online]. Available: https://cds.cern.ch/record/ 331068.

[49] S. Fartoukh *et al.*, "LHC Configuration and Operational Scenario for Run 3," CERN, Geneva, Tech. Rep., 2021. [Online]. Available: https://cds.cern.ch/ record/2790409.

[50] C. Service graphique, "Overall view of the LHC. Vue d'ensemble du LHC," 2014, General Photo. [Online]. Available: https://cds.cern.ch/record/1708849.

[51] B. Acharya *et al.*, "The physics programme of the moedal experiment at the lhc," *International Journal of Modern Physics A*, vol. 29, no. 23, p. 1 430 050, 2014. DOI: 10.1142/S0217751X14300506. eprint: https://doi.org/10.1142/ S0217751X14300506. [Online]. Available: https://doi.org/10.1142/S0217751X14300506.

[52] J. Pinfold, *Moedal-mapp, an lhc dedicated detector search facility*, 2023. arXiv: 2209.03988 [hep-ph].

[53] G. Anelli *et al.*, "The totem experiment at the cern large hadron collider," *Journal of Instrumentation*, DOI: 10.1088/1748-0221/3/08/S08007. [Online]. Available: https://dx.doi.org/10.1088/1748-0221/3/08/S08007.

[54] J. L. Feng, I. Galon, F. Kling, and S. Trojanowski, "Forward search experiment at the lhc," *Physical Review D*, DOI: 10.1103/PhysRevD.97.035001. [Online]. Available: https://dx.doi.org/10.1103/PhysRevD.97.035001.

[55] A. A. A. Jr. *et al.*, "The lhcb detector at the lhc," *Journal of Instrumentation*, DOI: 10.1088/1748-0221/3/08/S08005. [Online]. Available: https://dx.doi.org/ 10.1088/1748-0221/3/08/S08005.

[56] L. Collaboration, *Snd@lhc: The scattering and neutrino detector at the lhc*, 2023. arXiv: 2210.02784 `[hep-ex]`.

[57] R Scrivens *et al.*, "Overview of the status and developments on primary ion sources at CERN*," 2011. [Online]. Available: https://cds.cern.ch/record/1382102.

[58] M. Benedikt, P. Collier, V Mertens, J. Poole, and K. Schindl, *LHC Design Report* (CERN Yellow Reports: Monographs). Geneva: CERN, 2004. DOI: 10.5170/CERN-2004-003-V-3. [Online]. Available: http://cds.cern.ch/record/823808.

[59] H. Bartosik and G. Rumolo, *Performance of the lhc injector chain after the upgrade and potential development*, 2022. arXiv: 2203.09202 `[physics.acc-ph]`.

[60] E. Lopienska, "The CERN accelerator complex, layout in 2022.," 2022, General Photo. [Online]. Available: https://cds.cern.ch/record/2800984.

[61] D. Boussard and T. P. R. Linnecar, "The LHC Superconducting RF System," CERN, Geneva, Tech. Rep., 1999. [Online]. Available: https://cds.cern.ch/record/410377.

[62] L. Rossi, "The LHC superconducting magnets," *Conf. Proc. C*, vol. 030512, p. 141, 2003.

[63] S Baird, "Accelerators for pedestrians; rev. version," CERN, Geneva, Tech. Rep., 2007. [Online]. Available: https://cds.cern.ch/record/1017689.

[64] K. Schindl, "The Injector Chain for the LHC; rev. version," 1999. [Online]. Available: https://cds.cern.ch/record/384396.

[65] P. Grafström and W. Kozanecki, "Luminosity determination at proton colliders," *Progress in Particle and Nuclear Physics*, vol. 81, pp. 97–148, 2015, ISSN: 0146-6410. DOI: https://doi.org/10.1016/j.ppnp.2014.11.002. [Online]. Available: https://www.sciencedirect.com/science/article/pii/S0146641014000878.

[66] B. Schmidt, "The high-luminosity upgrade of the lhc: Physics and technology challenges for the accelerator and the experiments," *Journal of Physics: Conference Series*, vol. 706, no. 2, p. 022002, 2016. DOI: 10.1088/1742-6596/706/2/022002. [Online]. Available: https://dx.doi.org/10.1088/1742-6596/706/2/022002.

[67] O. Brüning and L. Rossi, "The high-luminosity large hadron collider," *Nature Reviews Physics*, vol. 1, Mar. 2019. DOI: 10.1038/s42254-019-0050-6.

[68] R. e. a. Tomás, "Operational scenario of first high luminosity LHC run," *JACoW*, vol. IPAC2022, pp. 1846–1849, 2022. DOI: 10.1088/1742-6596/2420/1/012003.

[69] C. Wong, *Introduction to High-energy Heavy-ion Collisions* (Introduction to High-energy Heavy-ion Collisions). World Scientific, 1994, ISBN: 9789810202637.

[70] G. Aad *et al.*, "Alignment of the ATLAS Inner Detector in Run-2," *Eur. Phys. J. C*, vol. 80, no. 12, p. 1194, 2020, 61 pages in total, author list starting page 45, 26 figures, 4 tables, published in EPJC. All figures including auxiliary figures are available at http://atlas.web.cern.ch/Atlas/GROUPS/PHYSICS/PAPERS/IDTR-2019-05. DOI: 10.1140/epjc/s10052-020-08700-6. arXiv: 2007.07624. [Online]. Available: https://cds.cern.ch/record/2724037.

[71] P. Krieger, "The atlas liquid argon calorimeter: Construction, integration, commissioning and performance from selected particle beam test results," vol. 2, Nov. 2005, pp. 1029 –1033, ISBN: 0-7803-9221-3. DOI: 10.1109/NSSMIC.2005. 1596428.

[72] M. Livan and R. Wigmans, *Misconceptions about calorimetry*, 2017. arXiv: 1704. 00661 [physics.ins-det].

[73] A. M. Henriques Correia, "The ATLAS Tile Calorimeter," CERN, Geneva, Tech. Rep., 2015. DOI: 10.1109/ANIMMA.2015.7465554. [Online]. Available: https://cds.cern.ch/record/2004868.

[74] G. Aad *et al.*, "Readiness of the ATLAS tile calorimeter for LHC collisions," *The European Physical Journal C*, vol. 70, no. 4, pp. 1193–1236, 2010. DOI: 10.1140/epjc/s10052-010-1508-y. [Online]. Available: https://doi.org/10. 1140%2Fepjc%2Fs10052-010-1508-y.

[75] G. Aielli *et al.*, "The rpc first level muon trigger in the barrel of the atlas experiment," *Nuclear Physics B - Proceedings Supplements*, vol. 158, pp. 11–15, 2006, Proceedings of the 8th International Workshop on Resistive Plate Chambers and Related Detectors, ISSN: 0920-5632. DOI: https://doi.org/10.1016/j. nuclphysbps.2006.07.031. [Online]. Available: https://www.sciencedirect.com/ science/article/pii/S0920563206004178.

[76] T. Argyropoulos *et al.*, "Cathode strip chambers in atlas : Installation, commissioning and in situ performance," in *2008 IEEE Nuclear Science Symposium Conference Record*, 2008, pp. 2819–2824. DOI: 10.1109/NSSMIC.2008.4774958.

[77] J. Pequenao, "Computer generated image of the ATLAS Muons subsystem," 2008. [Online]. Available: https://cds.cern.ch/record/1095929.

[78] M. Aaboud *et al.*, "Performance of the ATLAS Trigger System in 2015. Performance of the ATLAS Trigger System in 2015," *Eur. Phys. J. C*, vol. 77, no. 5, p. 317, 2017, 77 pages in total, author list starting page 61, 50 figures, 1 table. Published in Eur. Phys. J. C. All figures including auxiliary figures are available at http://atlas.web.cern.ch/Atlas/GROUPS/PHYSICS/PAPERS/TRIG-2016-01/. DOI: 10.1140/epjc/s10052-017-4852-3. arXiv: 1611.09661. [Online]. Available: https://cds.cern.ch/record/2235584.

[79] C. Bierlich *et al.*, "A comprehensive guide to the physics and usage of PYTHIA 8.3," *SciPost Phys. Codebases*, p. 8, 2022. DOI: 10.21468/SciPostPhysCodeb.8. [Online]. Available: https://scipost.org/10.21468/SciPostPhysCodeb.8.

[80] N. Desai and P. Z. Skands, "Supersymmetry and generic BSM models in pythia 8," *The European Physical Journal C*, vol. 72, no. 12, 2012. DOI: 10.1140/epjc/s10052-012-2238-0. [Online]. Available: https://doi.org/10.1140%2Fepjc%2Fs10052-012-2238-0.

[81] B. C. Allanach, "SOFTSUSY: a program for calculating supersymmetric spectra," *Comput. Phys. Commun.*, vol. 143, pp. 305–331, 2002. DOI: 10.1016/S0010-4655(01)00460-X. arXiv: hep-ph/0104145 [hep-ph].

[82] B. C. Allanach, S. P. Martin, D. G. Robertson, and R. R. de Austri, "The Inclusion of Two-Loop SUSYQCD Corrections to Gluino and Squark Pole Masses in the Minimal and Next-to-Minimal Supersymmetric Standard Model: SOFTSUSY3.7," 2016. arXiv: 1601.06657 [hep-ph].

[83] B. Allanach *et al.*, "SUSY les houches accord 2," *Computer Physics Communications*, vol. 180, no. 1, pp. 8–25, 2009. DOI: 10.1016/j.cpc.2008.08.004. [Online]. Available: https://doi.org/10.1016%2Fj.cpc.2008.08.004.

[84] A Salzburger, S Todorova, and M Wolter, "The ATLAS Tracking Geometry Description," CERN, Geneva, Tech. Rep., 2007, All figures including auxiliary figures are available at https://atlas.web.cern.ch/Atlas/GROUPS/PHYSICS/PUBNOTES/ATL-SOFT-PUB-2007-004. [Online]. Available: https://cds.cern.ch/record/1038098.

[85] M. Bandieramonte, R. M. Bianchi, J. Boudreau, A. Dell'Acqua, and V. Tsulaia, "The GeoModel tool suite for detector description," CERN, Geneva, Tech. Rep., 2021. DOI: 10.1051/epjconf/202125103007. [Online]. Available: http://cds.cern.ch/record/2773096.

[86] A. Collaboration, *Athena*, version 22.0.1, Apr. 2019. DOI: 10.5281/zenodo.2641997. [Online]. Available: https://doi.org/10.5281/zenodo.2641997.

[87] V. V. Uzhinsky, "The Fritiof (FTF) Model in Geant4," in *International Conference on Calorimetry for the High Energy Frontier*, 2013, pp. 260–264.

[88] D. Wright and M. Kelsey, "The geant4 bertini cascade," *Nuclear Instruments and Methods in Physics Research Section A: Accelerators, Spectrometers, Detectors and Associated Equipment*, vol. 804, pp. 175–188, 2015, ISSN: 0168-9002. DOI: https://doi.org/10.1016/j.nima.2015.09.058. [Online]. Available: https://www.sciencedirect.com/science/article/pii/S0168900215011134.

[89] V. N. Ivanchenko, O Kadri, M Maire, and L Urban, "Geant4 models for simulation of multiple scattering," *Journal of Physics: Conference Series*, vol. 219, no. 3, p. 032045, 2010. DOI: 10.1088/1742-6596/219/3/032045. [Online]. Available: https://dx.doi.org/10.1088/1742-6596/219/3/032045.

[90] A. Bagulya, M. Vladimirov, V. Ivanchenko, and N. Starkov, "Heavy-particle energy loss simulation using the geant4 toolkit," *Bulletin of the Lebedev Physics Institute*, vol. 36, no. 5, 127 – 134, 2009. DOI: 10.3103/S1068335609050017. [Online]. Available: https://www.scopus.com/inward/record.uri?eid=2-s2.0-77953130684&doi=10.3103%2fS1068335609050017&partnerID=40&md5=8d29c2988c9f88fc5c491aad10a024a0.

[91] Y. Fukuda *et al.*, "Neutrino-induced upward stopping muons in super-kamiokande," *Physics Letters B*, vol. 467, no. 3-4, pp. 185–193, 1999. DOI: 10.1016/s0370-2693(99)01188-0. [Online]. Available: https://doi.org/10.1016%2Fs0370-2693%2899%2901188-0.

[92] R. Chytracek, J. McCormick, W. Pokorski, and G. Santin, "Geometry description markup language for physics simulation and analysis applications.," *IEEE Trans. Nucl. Sci.*, vol. 53, p. 2892, 2006. DOI: 10.1109/TNS.2006.881062.

[93] H Takai and (for the ATLAS Collaboration), "Heavy ion physics with the atlas detector," *Journal of Physics G: Nuclear and Particle Physics*, vol. 30, no. 8, S1105, 2004. DOI: 10.1088/0954-3899/30/8/068. [Online]. Available: https://dx.doi.org/10.1088/0954-3899/30/8/068.

Appendix A: Number of Stopped Staus

$M_{1/2}$ GeV	% Stopped
300	$3689/413757 = 0.89\%$
400	$982/142370 = 0.69\%$
500	$192/61957 = 0.31\%$
600	$144/31062 = 0.46\%$
700	$46/17145 = 0.27\%$
800	$27/10133 = 0.27\%$
900	$16/6315 = 0.25\%$
1000	$11/4105 = 0.27\%$
1100	$6/2757 = 0.22\%$
1200	$7/1907 = 0.37\%$
1300	$3/1351 = 0.22\%$

Table A.1: The percentage of produced staus that are trapped in the ATLAS detector in simulation. The number of produced staus is based on the maximum cross section provided by pythia for that parameter value and the expected run 4 integrated luminosity of 715 fb^{-1}

Appendix B: LHC Cryogenics During Beam Fill
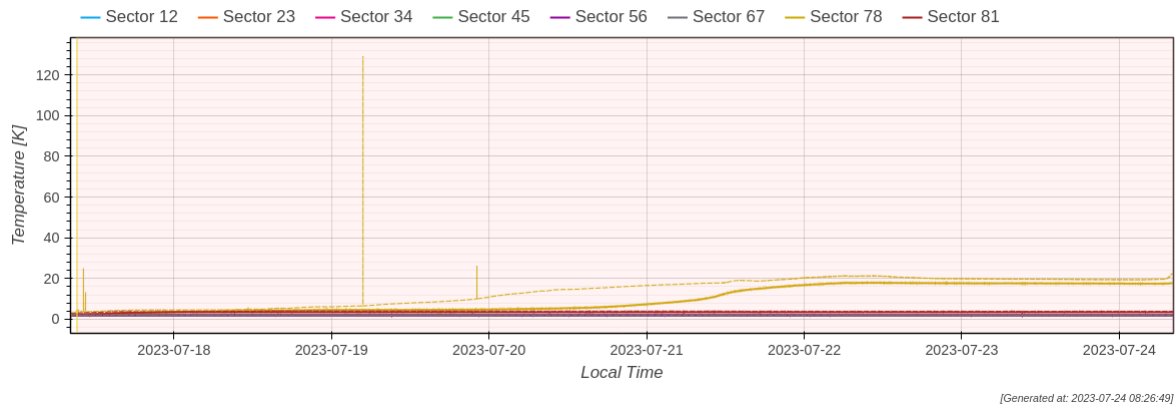
Figure B.1: The cryogenic status at the LHC, for the time period shown in figure 5.9. Cryogenic cooling is maintained during short periods of beam inactivity.

Appendix C: The Total Detected Events in the ADAM Detector

M_{12} \\ τ	7		30		90		150		365	
	Year end	Beam fill	Year end	Beam fill	Year end	Beam fill	Year end	Beam fill	Year end	Beam fill
300	0	99.7 ± 0.4	36.2 ± 0.3	94.2 ± 0.4	365.1 ± 0.6	80.0 ± 0.4	639.8 ± 0.8	70.5 ± 0.3	1142 ± 1	55.3 ± 0.3
400	0	26.4 ± 0.3	9.7 ± 0.2	25.0 ± 0.3	96.7 ± 0.5	21.3 ± 0.3	174.4 ± 0.6	18.7 ± 0.2	300.2 ± 0.7	14.6 ± 0.2
500	0	5.2 ± 0.2	2.0 ± 0.2	5.0 ± 0.2	20.8 ± 0.4	4.2 ± 0.2	38.0 ± 0.5	3.5 ± 0.2	62.1 ± 0.6	2.9 ± 0.2
600	0	3.9 ± 0.2	0.94 ± 0.09	3.7 ± 0.2	13.9 ± 0.4	3.0 ± 0.2	25.6 ± 0.5	2.8 ± 0.2	45.5 ± 0.5	2.2 ± 0.2
700	0	1.3 ± 0.2	0.10 ± 0.05	1.2 ± 0.2	3.6 ± 0.3	1.1 ± 0.2	7.6 ± 0.4	0.9 ± 0.2	13.4 ± 0.5	0.8 ± 0.2
800	0	0.7 ± 0.2	0.01 ± 0.02	0.8 ± 0.2	1.2 ± 0.3	0.7 ± 0.2	3.1 ± 0.4	0.6 ± 0.2	7.6 ± 0.5	0.4 ± 0.2
900	0	0.5 ± 0.2	0.3 ± 0.2	0.4 ± 0.2	2.5 ± 0.4	0.3 ± 0.2	3.9 ± 0.5	0.3 ± 0.2	6.1 ± 0.5	0.2 ± 0.2
1000	0	0.3 ± 0.2	0.04 ± 0.07	0.3 ± 0.2	1.0 ± 0.3	0.3 ± 0.2	1.9 ± 0.4	0.2 ± 0.2	3.4 ± 0.5	0.2 ± 0.2
1100	0	0.2 ± 0.2	0.3 ± 0.2	0.2 ± 0.2	1.7 ± 0.5	0.1 ± 0.2	2.4 ± 0.5	0.1 ± 0.2	4.0 ± 0.5	0.05 ± 0.09
1200	0	0.2 ± 0.2	0	0.2 ± 0.2	0.6 ± 0.3	0.2 ± 0.2	1.6 ± 0.5	0.2 ± 0.2	3.3 ± 0.5	0.1 ± 0.2
1300	0	0.1 ± 0.2	0.00 ± 0.02	0.1 ± 0.2	0.5 ± 0.4	0.1 ± 0.2	0.8 ± 0.5	0.1 ± 0.2	0.8 ± 0.4	0.1 ± 0.2

Table C.1: The detectable stau decays, e.g. those occurring during beam-off times, for given parameters. "Year end" refers to detections during the year-end shutdowns, and "Beam fill" refers to decays detected during short stops during the beam fill cycle as described in section 5.3.1. The random one hour beam fill intervals and stau creation times are chosen and applied to the data 1000 times to determine the number of new detection opportunities and the results are averaged. Values of zero with no uncertainty mean that for each of the 100 trials the result was identically zero.

τ / M12	7	30	90	150	365
300	11.7 ± 0.5	11.4 ± 0.4	11.8 ± 0.2	10.7 ± 0.2	11.05 ± 0.08
400	15 ± 2	16 ± 2	10.8 ± 0.4	13.3 ± 0.3	13.4 ± 0.2
500	14 ± 7	10 ± 5	10 ± 2	19 ± 2	15.4 ± 0.7
600	20 ± 20	14 ± 8	22 ± 3	13 ± 2	15.1 ± 0.9
700	20 ± 30	20 ± 30	7 ± 6	17 ± 5	17 ± 3
800	20 ± 60	20 ± 50	10 ± 20	7 ± 8	4 ± 3
900	30 ± 100	20 ± 60	20 ± 20	20 ± 10	18 ± 7
1000	10 ± 90	0 ± 200	40 ± 50	20 ± 20	30 ± 20
1100	0 ± 300	0 ± 50	10 ± 20	20 ± 20	40 ± 20
1200	0 ± 200	0 ± 200	0 ± 20	20 ± 30	12 ± 10
1300	0	0	0	0	0

Table C.2: The percent efficiency of the ADAM detector for detecting decays which have occurred during background free periods under different $M_{1/2}$ and lifetime (τ) values. For low $M_{1/2}$ the results indicate the ADAM detector would be successful at detecting the decays of stau particles. At high $M_{1/2}$ in many cases there are zero events, and due to the low statistics, the uncertainty "blows up" encapsulating the entire scale. This is due to the low cross section for these parts of the parameter space as shown in figure 5.2.

Appendix D: Uncertainty Calculations

D.1   Binomial Distribution

In our study, we encounter scenarios where the outcome of an event can be categorized into success or failure. This includes: whether a particle stops, decays within a time window (i.e., in-time decays), or is detected. These outcomes can be modelled using the binomial distribution.

Let p be the probability of success (e.g., a particle stopping), and n be the number of trials (e.g., the total number of particles). Then, the probability mass function of the binomial distribution is given by:

$$P(X = k) = \binom{n}{k} p^k (1 - p)^{n-k} \tag{D.1}$$

where k is the number of successes.

D.2   Standard Deviation and Standard Error of the Binomial Distribution

The standard deviation of a binomial distribution is given by:

$$\sigma = \sqrt{n \cdot p \cdot (1 - p)} \tag{D.2}$$

where n is the number of trials, and p is the probability of success. This represents the spread of the distribution.

Considering three successive binomial processes: stopping, in-time decay, and detection, we define the following variables:

- N: Total number of particles produced.

- S: Number of particles that stop.

- T: Number of particles that decay in time.

- D: Number of particles detected.

The probabilities for each process are given by:

$$\epsilon_S = \frac{S}{N}, \quad \epsilon_T = \frac{T}{S}, \quad \epsilon_D = \frac{D}{T}$$

Using the probability of a particle stopping as an example we can substitute $p = \epsilon_S = S/N$ into equation D.2.

$$\sigma_{\epsilon_S} = \sqrt{S(1 - S/N)} \tag{D.3}$$

The standard error (SE) for a standard deviation (σ) and number of trials (n) is given by

$$SE = \frac{\sigma}{\sqrt{n}} \tag{D.4}$$

Using this with equation D.3 we get the standard error on the number of particles which stop in the ATLAS detector

$$SE_{\epsilon_S} = \sqrt{\frac{S\,(1 - S/N)}{N}} \tag{D.5}$$

Similarly, the uncertainty for the probability of a stopped particle S to decay during a monitoring time window T is

$$SE_{\epsilon_T} = \sqrt{\frac{T\,(1 - T/S)}{S}} \tag{D.6}$$

and the probability of a detection D, given a decay occurring during a monitoring time window T is

$$SE_{\epsilon_D} = \sqrt{\frac{D\left(1 - D/T\right)}{T}} \qquad (D.7)$$

D.3 Standard Deviation of the Mean

As described in sections 4.2 and 5.4, the particle creation times and short monitoring windows are assigned randomly 1000 times and the resulting number of in-time decays and detections are averaged. For these processes, there is also a random error associated. The standard deviation of the mean for these quantities is given by

$$\sigma = \sqrt{\frac{1}{n-1} \sum_{i=1}^{n} (x_i - \bar{x})^2} \qquad (D.8)$$

where n is the number of trials, x_i the random variable and $\bar{x}$ the mean. The standard error is then given by equation D.4.

D.4 Propagation of Uncertainties

The uncertainty on a multivariate function $f\left(A, B, C\right)$ is

$$SE_f = f\sqrt{\left(\frac{SE_A}{A}\right)^2 + \left(\frac{SE_B}{B}\right)^2 + \left(\frac{SE_C}{C}\right)^2} \qquad (D.9)$$

When applying this to the total recorded events from those decays which have happened during a monitoring time window (as shown in table 5.2), which requires a produced particle to 1. stop in the detector 2. decay during a monitored time window and 3. be detected by ADAM, we have:

$$SE_{\epsilon_{\text{overall}}}(\%) = D\sqrt{\frac{SE_{\epsilon_S}^2}{S^2} + \frac{SE_{\epsilon_T}^2}{T^2} + \frac{SE_{\epsilon_D}^2}{D^2} + \frac{SE_{\epsilon_t}^2}{1000^2} + \frac{SE_{\epsilon_d}^2}{1000^2}} \qquad (D.10)$$

where the terms SE_{ϵ_t} and SE_{ϵ_d} represent the standard deviations of the average number of in-time decays and the average number of particle detections when

randomly assigning the particle creation times and monitoring windows 1000 times.